Department of Precision and Microsystems Engineering

Characterization of Wrinkles and Quantum Emitters in 2D Hexagonal Boron Nitride for Optofluidic Applications

Tetsuo Martynowicz

Report no : 2025.006
Coach : Dr. Sabina Caneva
Professor : Prof. dr. Peter Steeneken
Specialisation : DMN
Type of report : Master thesis
Date : 18 February 2025

Characterization of Wrinkles and Quantum Emitters in 2D Hexagonal Boron Nitride for Optofluidic Applications

MSc. Thesis

by

Tetsuo Martynowicz

Tuesday 18th February, 2025

Senior supervisor:	Dr S. Caneva
Daily supervisor:	X. Yang, PhD candidate
Department:	Precision and Microsystems Engineering
Faculty:	Faculty of Mechanical Engineering, TU Delft

TU Delft

Characterization of Wrinkles and Quantum Emitters in 2D Hexagonal Boron Nitride for Optofluidic Applications

MSc. Thesis

by

Tetsuo Martynowicz

to obtain the degree of Master of Science
at Delft University of Technology,
to be defended publicly on Monday February 24, 2025 at 10:30 AM.

Student number:	4957342	
Thesis committee:	Dr S. Caneva,	Senior supervisor
	X. Yang, PhD candidate	Daily supervisor

TU Delft

Preface

Presented here is my master's thesis on the characterization of wrinkles and quantum Emitters in 2D hexagonal boron nitride for optofluidic applications. This report marks the conclusion of my final research project and the completion of my master's program in Mechanical Engineering, specializing in High Tech Engineering, at Delft University of Technology. I began this research in December 2023 with a literature review and carried out an experimental phase from March 2024 to February 2025.

In my undergraduate studies, and even during the initial phase of my master's, I was not particularly drawn to nanotechnology; it simply was not on my radar. However, that changed after taking the 'Introduction to Nanoscience and Technology' course, where I was introduced to the fundamentals of quantum mechanics and advanced measurement techniques like electron and atomic force microscopy. Fascinated by these concepts, a few months later I reached out to the course instructor, Sabina Caneva, for a master thesis project. She proposed a project on deterministic quantum emitter engineering in hexagonal boron nitride, a 2D material. I quickly became engaged and decided to commit the second year of my master's to this research. Looking back, my interest in this topic only grew and I developed a passion for experimental work and research in nanotechnology. Through this project I developed a deep understanding of the intricacies involved in working at the micro- and nanometer scale, and I gained hands-on experience with various fabrication and characterization techniques. But perhaps more importantly, I had a lot of fun. Obviously, the journey presented its many challenges, but I was fortunate to have the support of many others along the way.

I sincerely thank my supervisors Sabina Caneva and Xiliang Yang, for their guidance throughout this project. Sabina was incredibly supportive and offered guidance whilst also allowing me to follow my own path. Xiliang provided tremendous help with the experimental work in the lab and was always willing to discuss my results and address any issues that arose. I also wish to thank everyone in the Caneva Lab group for the enjoyable moments and constructive feedback. Finally, my heartfelt thanks go to my girlfriend Anne, my dear friends Pepijn, Rolf, Abel, Niels, Fabian, Maurita, Jeroen, and all other friends and family.

Tetsuo Martynowicz
Delft, February 2025

Abstract

Understanding the relationship between the sequence, structure, and function of biomolecules, which can serve as biomarkers for early disease detection, is vital for advancing molecular diagnostics. Consequently, highly sensitive optical readout methods to identify biomolecules, such as proteins, are being developed. Single-molecule Förster resonance energy transfer (smFRET) has recently emerged as a promising technique for accurately identifying low-abundance proteins in samples as small as a single cell. However, the effectiveness of this fluorescence-based method depends on the precise design of donor-acceptor probe pairs to sequence labelled proteins. Recent advances have introduced the use of optically active atomic defects in two-dimensional hexagonal boron nitride (2D h-BN), also known as quantum emitters, as promising donor probes. Yet, achieving control over their spatial and spectral properties remains a significant challenge. This thesis investigates thermally induced wrinkles in exfoliated 2D h-BN crystals as potential nanochannels for the localization of both quantum emitters and biomolecules, the latter typically being in solution. The study reveals that the formation and morphology of these wrinkles are strongly influenced by the mismatch in thermal expansion coefficient between h-BN and its substrate. Additionally, the wrinkles exhibit variations in strain and effectively localize quantum emitters in the visible range. Initial experiments with water and ethanol provided a first indication of solution-based effects on wrinkle and emitter properties. The wrinkles remained stable upon exposure and even swelled, suggesting liquid uptake. Additionally, both liquids enhanced the fluorescence intensity of emitters on the wrinkles without necessarily activating those on the flat regions of the h-BN flakes. These findings highlight new research opportunities for using wrinkled 2D h-BN in optofluidic applications, potentially advancing the integration of quantum emitters in smFRET-based sensing devices.

Contents

1 Introduction

Understanding the sequence-structure-function relationship of biomolecules is a key challenge in modern bionanoscience, particularly in molecular diagnostics. Biomolecules like DNA and proteins play crucial roles in cellular function and can serve as biomarkers for early disease detection. While DNA sequencing is now rapid, affordable, and high-throughput, protein sequencing remains significantly more complex. Unlike DNA, which consists of four bases, proteins are made up of 20 amino acids with various modifications, making real-time sequencing far more challenging. Current protein sequencing methods, such as mass spectrometry, struggle to detect the full range of protein concentrations in biological samples and often require large volumes, limiting the analysis of low-abundance proteins. These challenges highlight the need for new high-sensitivity technologies capable of comprehensive protein analysis.

One promising approach beyond direct sequencing is fingerprinting, which requires only partial sequence information for protein identification [1]. This can be achieved by optically detecting a labelled subset of the amino acid chain using fluorescence-based techniques. By comparing the readout with a database, the protein can be identified with an accuracy of up to 90%. In this context, single-molecule Förster Resonance Energy Transfer (smFRET) has emerged as a powerful tool for tracking fluorescence variations between donor-acceptor probe pairs, utilizing its nanometer-scale sensitivity to measure molecular interactions [2]. The success of fingerprinting with smFRET depends on the precise design of these probes, and recent developments in probe materials have expanded beyond organic dyes to include fluorescent proteins, inorganic nanoparticles, and more recently, 2D materials [3].

Among these 2D materials, hexagonal boron nitride (h-BN) has gained attention due to its wide 6 eV bandgap, which can host sub-bandgaps arising from unique crystallographic defects [4]. When excited by sufficiently energetic light, these defects can act as ultra-bright, stable optical emitters also known as quantum emitters. Additionally, h-BN is not toxic to biological samples and remains stable in liquid environments and harsh chemical conditions, making it a promising platform for FRET-based donor probes. However, the photophysical properties of h-BN defects are not yet fully understood, and current fabrication methods still lack precise spatial and spectral control over the emitters.

This controllability is essential, as FRET only occurs under specific conditions. For FRET, there must be an overlap between the emission and excitation spectra of the donor and acceptor probe. Additionally, FRET efficiency decreases sharply with increasing distance between donor and acceptor probe, following an inverse power-law relationship. To address these challenges, strain engineering in the form of wrinkling shows potential for localizing both quantum emitters and biomolecules. These nanochannels may guide proteins labelled with fluorescent acceptor probes into close proximity with the donor emitters concentrated along the wrinkles, thereby enabling FRET between the two.

The purpose of this report is to characterize the structural properties of wrinkles in 2D hexagonal boron nitride and to explore the optical properties of emitters that may be localized on these out-of-plane features. Additionally, this research is extended to an optofluidic context by exposing the wrinkles to liquid, considering that biomolecules are typically in solution.

2
Theoretical Framework

This chapter aims to provide a comprehensive explanation of fundamental concepts essential for understanding the working principle of a FRET-based single-molecule fingerprinting technique using quantum emitters in 2D materials.

2.1. Fluorescence

Fluorescence is a form of luminescence, which is the emission of light by a substance that is brought in an electronically excited state by the absorption of light. The emitted light is released when the excited electrons fall back to their ground state. One widely encountered fluorescent substance is quinine, which is present in tonic water. When exposed to ultraviolet light from the sun, quinine in tonic water becomes excited. Upon returning to its ground state, quinine emits blue light with a wavelength around 450 nm as shown in Figure 2.1. Sir John Frederick William Herschel first reported the observation of fluorescence from a quinine solution in sunlight in 1845 [5].

Figure 2.1: Tonic water containing quinine molecules illuminated by ultraviolet light (Cathy Scola, Getty Images).

2.1.1. Principles of Fluorescence

Fluorescence involves electronic transitions which are described below and can be represented in an energy diagram as shown Figure 2.2.

1. **Excitation** - An electron in quantum mechanical systems such as molecules or atoms tends to exist in the lowest vibrational level of the ground state $\mathbf{S_0}$ (un-excited state). When this electron in the ground state is excited through the absorption of photons from an external light source, it moves to a higher energy state $\mathbf{S_1}$ (excited state). Upon excitation, the electron is brought in a high vibrational level of the excited state according to the Franck-Condon principle, which states that an electronic transition from one vibrational level to another is more likely to happen if two vibrational wavefunctions overlap more significantly [6].
2. **Vibrational relaxation** - The excited electron thereafter relaxes to the lowest vibrational level of the excited state and gives up some energy to its surroundings on a short time scale of 10^{-14} -

10^{-12} s. This relaxation usually occurs non-radiatively, meaning energy is not transferred through light but by other means such as phonons (units of vibrational energy).

3. **Fluorescence** - From the lowest vibrational level of the excited state, the electron may return to the ground state and emit a photon in the process via spontaneous emission [7]. This transition is vertical, which means that the electron probably does not immediately end up in the lowest vibrational state of the ground state. Due to the energy lost with vibrational relaxation, the emitted photon has a longer wavelength, and hence less energy, than the excitation photon. This phenomenon is also known as Stokes shift [8].
4. **Vibrational relaxation** - When the electron has landed in one of the vibrational levels of the ground state, it relaxes non-radiatively to the lowest vibrational level of the ground state.

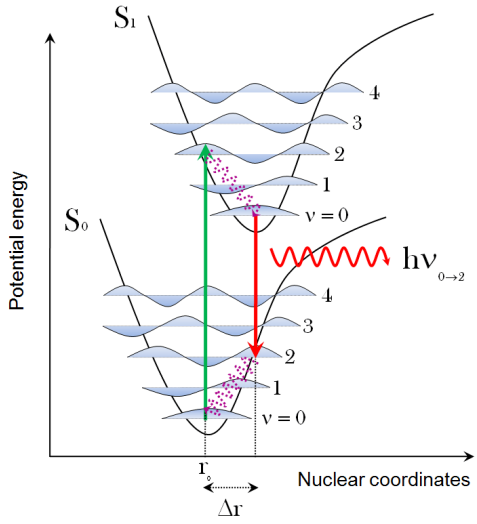

Figure 2.2: An energy diagram showing the potential energy curves of the ground singlet state $\mathbf{S_0}$ and first excited singlet state $\mathbf{S_1}$ with the discrete vibrational energy levels presented as waves. Excitation of the electron (green arrow) is most likely to occur between the vibrational wave functions that overlap the most, according to the Franck-Condon principle. After excitation, the electron relaxes non-radiatively (upper purple arrow) to the lowest vibrational level of the electronic state and successively decays to a vibrational level in the ground state, emitting a photon in the process (red arrow). Lastly, the electron relaxes to the lowest vibrational level of the ground state (lower purple arrow). Figure adapted from [9].

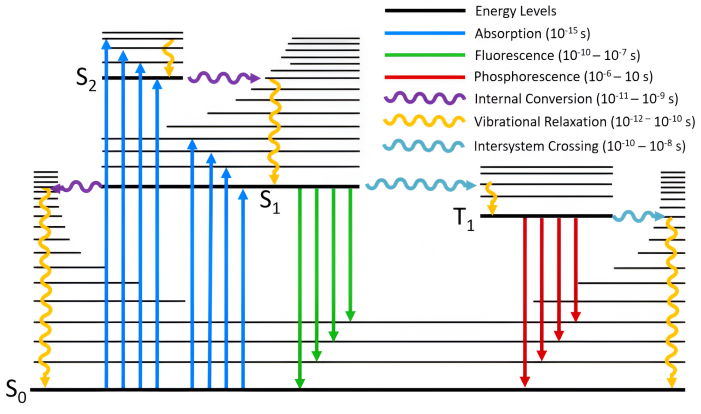

Figure 2.3: A typical Perrin-Jablonski diagram showing the possible radiative transitions (straight arrows) and non-radiative transitions (squiggly arrows) in a quantum mechanical system. The energy levels are shown by the horizontal black lines; with energy increasing along the vertical axis. The bold lines represent the lowest vibrational level of each electronic state, with the higher vibrational levels represented by thinner lines. The vibrational levels become more closely spaced as energy increases and eventually form a continuum. The naming of the electronic states is based on the spin angular momentum configuration of each state. Singlet states are denoted by an **S** and triplet states by **T**. Figure adapted from [10].

Absorption and Emission Spectra

The absorption and emission spectra of a fluorescent substance show the range of wavelengths at which these substances emit or absorb photons after being excited by an external energy source. Due to the rapidness of the vibrational relaxation steps, a general property of fluorescence is that the same emission spectrum is observed irrespective of the excitation wavelength, also known as Kasha's rule [11]. The typical fluorescence spectra of two different fluorescent substances: perylene and quinine, are shown in Figure 2.4. The spectral peaks originate from the return and excitation of electrons to different vibrational states of the ground and excited states thus revealing the energy spacing between the various vibrational energy levels. For perylene, the spacing of the vibrational energy levels of the excited states is similar to that of the ground state. As a result, the emission spectrum is a mirror image of the absorption spectrum. For quinine, the emission spectrum is different from its absorption spectrum due to excitation to the second excited state $\mathbf{S_2}$ and rapid relaxation to the lowest excited state $\mathbf{S_1}$. Since emission occurs predominantly from the lowest excited state $\mathbf{S_1}$, the total absorption spectrum is not mirrored.

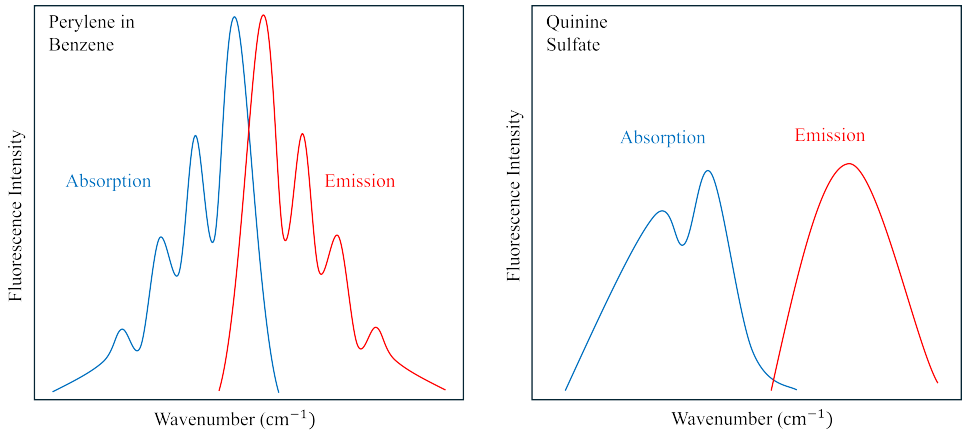

Figure 2.4: Illustrative absorption and emission spectra of perylene and quinine, based on figures from [12]. The emission spectrum of perylene is a mirror image of the absorption spectrum due to a similarity in the electronic transitions in emission and absorption, and a similarity in vibrational levels between $\mathbf{S_0}$ and $\mathbf{S_1}$. This is not the case for quinine as excitation happens from $\mathbf{S_0} \rightarrow \mathbf{S_2}$ whereas emission usually happens from $\mathbf{S_1} \rightarrow \mathbf{S_0}$. Therefore, the emission spectrum is not a mirror image of the total absorption spectrum for quinine.

Fluorescence Lifetime and Quantum Yield

The fluorescence lifetime and quantum yield are perhaps the most important characteristics of fluorescent substances. The fluorescence lifetime denotes the time an electron spends in the excited state and therefore determines the time available for a fluorescent substance to interact with or diffuse in its environment. The time scale (lifetime) of fluorescence is relatively fast (typically around 10^{-9} s) because the return of the electron to the ground state between singlet states is spin allowed. Another form of luminescence is phosphorescence, which is the emission of light from triplet excited states. Molecules in the $\mathbf{S_1}$ state can undergo a spin conversion to the first triplet state $\mathbf{T_1}$ through a process called internal conversion as shown in Figure 2.3. In principle, transitions from $\mathbf{T_1} \rightarrow \mathbf{S_0}$ are forbidden but they can still happen rarely. Therefore, phosphorescence happens on a much longer time scale (typically around 10^{-3} - 10^{3} s). Quantum yield is the number of photons emitted relative to the number of photons absorbed. Substances with the largest quantum yield, approaching unity, display the brightest emissions [12]. We note that the energy yield of fluorescence is always less than unity because of energy lost in vibrational relaxation.

2.1.2. Förster Resonance Energy Transfer

Förster resonance energy transfer (FRET) is a fluorescence-based measuring technique that involves distance dependent non-radiative energy transfer from a donor to an acceptor. The energy transfer takes place through long-range dipole-dipole interactions, which is analogous to the energy transfer between two coupled oscillators, such as a pair of tuning forks, vibrating at the same frequency [13]. The transfer of energy results in a decrease in both the fluorescence intensity and excited lifetime of the

donor, and an increase in the emission intensity of the acceptor. FRET is one of the few tools available for measuring nanometer scale distances and changes in distances, both in vitro and in vivo [14] making it interesting for biosensing applications. For FRET to occur, the following criteria are important to consider [13]:

1. **Spectral overlap interval:** This is referred to as the degree of overlap between the fluorescence emission spectra of the donor molecule and the absorption or excitation spectrum of the acceptor fluorophore. An overlap as shown in Figure 2.5a is required for FRET.
2. **Proximity:** This relates to the distance between the acceptor and the donor. As depicted in Figure 2.5b, the transfer rate varies with the 6^{th} power of the acceptor-donor separation distance R, over a range of 1-10 nm.
3. **Fluorescence lifetime:** This denotes the time that the donor spends in the excited state, which must be of sufficient duration to allow FRET to occur.

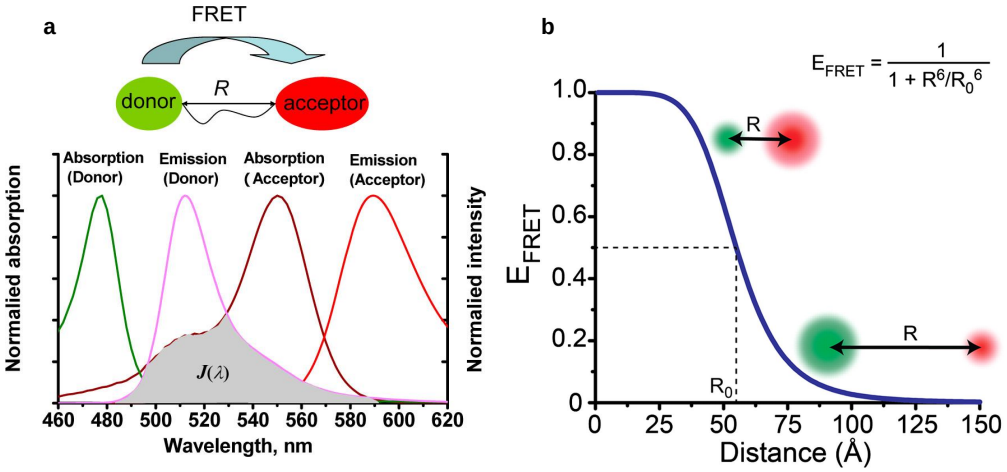

Figure 2.5: **(a)** Diagram showing the fluorescence absorption and emission spectra of a donor and acceptor and their overlap integral. Figure adapted from [15]. **(b)** Diagram showing the relation between the FRET efficiency (E_{FRET}) and the distance (R) between donor and acceptor. Figure adapted from [16]. The energy transfer rate varies with the 6^{th} power of separation distance, the closer the donor and emitter are the higher the energy transfer rate.

Thus far, the principles of fluorescence and FRET have been addressed. In Section 2.2, Examples of fluorescent substances and substances suitable as donors and acceptors for FRET will be provided.

2.2. Quantum Emitters

Quantum emitters are examples of substances that exhibit fluorescence. These photon sources can be broadly classified into two categories [17]: **1)** excitonic emitters in which the quantum emission occurs through a near bandgap transition and **2)** defect-based emitters which have sub bandgaps between the valence and conduction band of the bulk material. Recently, the focus in research has shifted from emitters in 3D solid state hosts, which was reaching saturation partly due to physical limitations, to the exploration of atomically thin 2D materials where new emitters have been discovered.

2.2.1. Examples of Quantum Emitters

Quantum emitters can occur naturally as fluorophores, or atomic defects in crystal lattices, but can also be engineered with greater control over the properties of the emitters to tailor them for specific applications. Based on the characteristics of the emitter, emitted photons can exhibit unique quantum properties, such as entanglement and superposition, making quantum emitters key components in various cutting-edge technologies such as quantum computing, -communications, -sensing, and fundamental science [18]. This list contains some of the most researched examples of quantum emitters:

1. **Fluorophores:** These are fluorescent chemical compounds which emit photons when exposed to an external light source. They can form covalent bonds with molecules, acting as markers or dyes for FRET-based measuring of biomolecule diffusion, conformational changes, and biomolecule-biomolecule interactions.
2. **Quantum dots:** These are defined as three dimensional structures so small that particles confined within the quantum dot experience quantum mechanical effects. In the context of this report, a quantum dot is defined as a semiconductor nanoparticle with an electronic bandgap. The bandgap is related to the allowed discrete energy levels within the quantum dot which arise from the size and shape of the structure. Among the best performing quantum dots are self-assembled epitaxial InAs-based quantum dots in GaAs which operate primarily at cryogenic temperatures.
3. **Colour centers in solid state crystals:** Solid state crystals are solid materials whose atoms appear in various highly ordered crystallographic configurations. The crystal lattice of some of these materials may include atomic defects such as missing atoms (vacancies), impurities (substitutions) or a combination of these which form sub-bandgaps between the valence and conduction band allowing for quantum emission. Some of these emitting defects (colour centers) are even stable at room temperature if the electronic ground and excited states are far from the crystal's valence and conduction bands, as is the case for hexagonal boron nitride. Among the most studied colour centers are the nitrogen-vacancy (NV) and the silicon-vacancy (SiV) in diamond [19][20]. These occur naturally in diamond and can also be produced by ion implantation and post-annealing [21].

2.2.2. Properties of Quantum Emitters

Table 2.1 contains a list of properties which are commonly used to describe the characteristics and performance of quantum emitters. Important critertia of donors and acceptors for biosensing applications and single-molecule FRET in particular are high brightness in the visible range, photostability, reproducibility, room temperature operation, high quantum yield and long fluorescence lifetime [3].

Table 2.1: Properties of quantum emitters [22] [12].

Property	Description
Brightness	This represents the maximum rate at which single photons can be extracted from the source on demand (photon counts per second).
Emission wavelength	This describes the wavelength of emitted light for which the intensity is maximum in the photoluminescence spectrum.
Linewidth	This is a measure of the bandwidth of frequencies (wavelengths) of photons emitted by the quantum emitter. The Full-Width-Half-Maximum (FWHM) of the photoluminescence spectra determines the emission linewidth.
Fluorescence lifetime	This quantifies the time for the emitter to return to its ground state after excitation.
Purity	This quantifies the singleness of photon emission and is defined by the value of the second-order autocorrelation function at zero time delay $g^2(0)$.
Photostability	Indicators of low photostability are a sudden fall or rise in photon counts when an emitter randomly switches on and off under long excitation times (blinking) and the loss of an emitter's ability to emit light (bleaching).
Quantum yield	This is the number of photons emitted relative to the number of photons absorbed.
Reproducibility	This means consistent properties across multiple emitters.
Operation temperature	This involves the temperature at which the emitter is optically active.

A photoluminescence spectrum like the one in Figure 2.6 can give insight into several properties of the quantum emitter including the brightness, wavelength and linewidth. The zero phonon line (ZPL) corresponds to the energy difference between the lowest vibrational level of the ground state and the

lowest vibrational energy level of the excited state, depicted by the smaller upwards arrow and larger downwards arrow in Figure 2.6a. The phonon side band (PSB) is the product of the interaction between the excited electron and phonons, which results in a broader curve with lower intensity in the emission spectrum. It is shifted left of the ZPL for fluorescence and right of the ZPL for absorption.

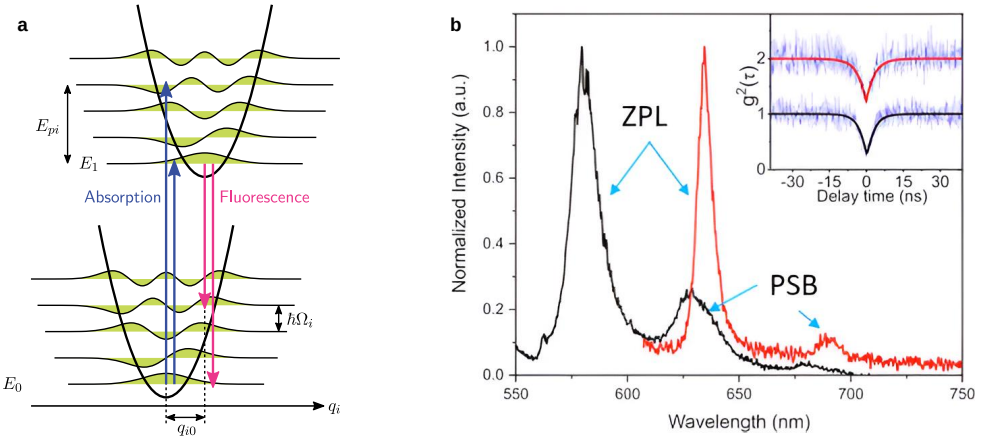

Figure 2.6: **(a)** Energy diagram displaying the electronic transitions for absorption with and without phonons (upward arrows) and the symmetric process for excitation (downward arrows), Figure adapted from [23]. **(b)** Photoluminescence spectra of two quantum emitters in h-BN showing the ZPL and the PSB. The inset displays the corresponding autocorrelation functions which are a measure of the quantum nature of the emitters. Figure adapted from [24].

As stated before in the introduction of Section 2.2, there has been a shift of focus in research from emitters in 3D solid state hosts to the exploration of atomically thin 2D materials. It is important to note that not all 2D materials can host quantum emitters and that there are major differences in the ones that do. This will be elaborated upon in section 2.3.

2.3. 2D Materials and Hexagonal Boron Nitride

Two-dimensional (2D) materials are defined as solid state crystals consisting of single- or few-layer atoms, in which the in-plane interatomic covalent bonds are much stronger than the weak van der Waals forces along the stacking direction [25]. The discovery of graphene has opened the way for studying 2D materials, with a predominant focus on their atomic structures, defects, mechanical behaviors and photophysical properties. Generally, 2D materials can be categorized into four types: the graphene family, Xenes, chalcogenides, and 2D nitrides/oxides [25]. Graphene is the most widely studied 2D material and displays specific metallic properties when it comes to electronic characteristics. However, it does not possess an electronic bandgap and therefore can not host quantum emitters. Alternatively, the wide electronic bandgap of hexagonal boron nitride (h-BN) and relatively smaller bandgap of transition metal dichalcogenides (TMDCs) make them promising quantum emitter hosts for applications in optical devices, phototransistors, and photodetectors [25]. An overview of various 2D material properties is given in Table 2.2.

2.3.1. Transition Metal Dichalcogenides

Transition metal dichalcogenides (TMDCs) are atomically thin semiconductors of the form MX_2, where M is a transition metal (such as molybdenum or tungsten) and X is a chalcogen atom (such as selenide or sulfur). As shown in Figure 2.7, the M and X atoms are covalently bonded to form an X-M-X sandwich structure within every monolayer. Depending on the arrangement of the atoms, the structures of monolayer TMDCs can be categorized, with trigonal prismatic (e.g. MoS_2 and WS_2) and octahedral (e.g. TiS_2) being the most common types [26]. A chalcogen - metal - chalcogen arrangement along the z-direction is considered as single layer, and weak van der Waals forces between each layer (chalcogen - chalcogen) enable breaking down bulk TMDCs to obtain a monolayer flake [27].

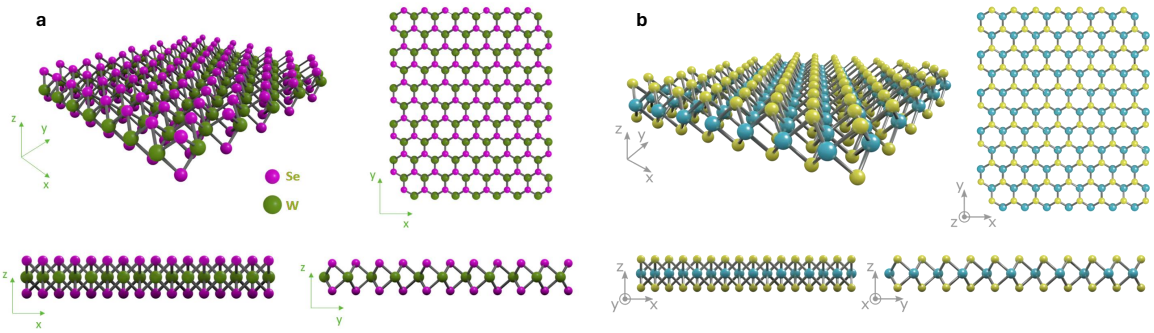

Figure 2.7: Crystal lattice structures of two TMDCs: **(a)** WSe_2 **(b)** MoS_2. Figures adapted from [28].

Properties

2D TMDCs present a wide variety of electronic properties ranging from insulating to semiconducting (e.g. MoS_2 and WSe_2) to metallic or semi-metallic (e.g. VSe_2 and TaS_2). The difference in electronic behaviour originates from the progressive filling of the non-bonding d-bands by the transition metal electrons [26]. The direct bandgap of semiconducting TMDCs can be exploited in electronics to create transistors [29] and in optics for the use in photodetectors [30]. 2D TMDCs are mechanically flexible and strong materials with a Young's modulus of 270 GPa and a breaking strength of 23 GPa for monolayer MoS_2 [31]. Additionally, they can easily be stacked with dissimilar TMDCs to construct a wide range of heterostructures with unique functions. The biocompatibility of TMDCs are often limited, as they can exhibit varying degrees of toxicity to biological samples, depending on the particular TMDC. It is suggested that the chalcogen atom might significantly influence its biocompatibility [32].

2.3.2. Hexagonal Boron Nitride

Boron nitride is a compound which consist of an equal amount of boron and nitrogen atoms which can be arranged in various crystal structures including hexagonal (h-BN), cubic (c-BN), wurtzite (w-BN) and amorphous (a-BN) [33]. Hexagonal boron nitride (h-BN) stands out as the most stable configuration among these arrangements at room temperature and normal pressure, featuring a stacking pattern where boron and nitrogen atoms alternate directly atop one another. The edge of a nanosheet can be either zigzag (B- or N-edged) or armchair (BN pair-edged) [34] as shown in Figure 2.8.

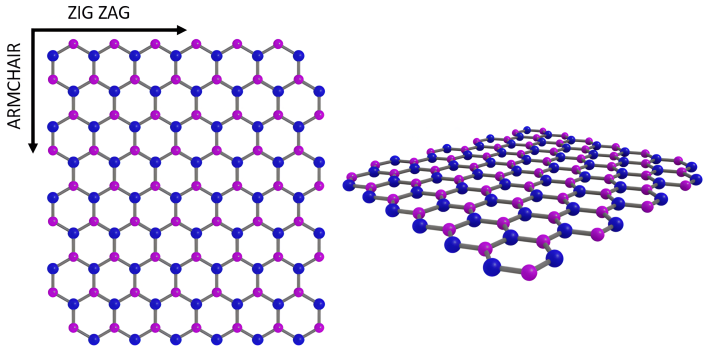

Figure 2.8: Crystal structure of monolayer hexagonal boron nitride with the zig zag and armchair directions indicated. Figure adapted from [35].

Properties

Hexagonal boron nitride exhibits an ultra wide indirect bandgap of ∼6 eV [36] and its dangling-bond free surface, insulating nature and thermal/chemical stability make it an ideal substrate for electronic devices. It is a remarkably robust material, being able to resist degradation in oxidizing environments at high temperature [37]. Mechanically, monolayer h-BN has a high Young's Modulus of 860 GPa and a fracture strength of 70.5 GPa [38]. Moreover, h-BN has generally been found to be biocompatible (i.e. not toxic) to cells [32].

Table 2.2: Properties of 2D materials [39][40][41][42][31][32][38].

Property	Unit	Graphene	MoS_2	WSe_2	h-BN
Structure	-	Hexagonal	Hexagonal	Hexagonal	Hexagonal
Electronic bandgap	eV	0	1.57	1.65	5.995
Young's modulus (monolayer)	GPa	1000	270 ±100	197-227	860
Strength (monolayer)	GPa	55	16-30	24.7-25.19	70.5
Biocompatibility	-	Medium	Medium	Low	High

2.3.3. Preparation of 2D Materials

The preparation method has an essential effect on the properties, structure and crystallinity of 2D nanosheets, and thereby on their application and performance [33]. The preparation of 2D materials involves two main approaches:

1. **Bottom-up:** Bottom-up methods entail growing or depositing a film onto a surface. Examples of bottom-up methods are chemical vapor deposition (see Figure 2.9a), physical vapor deposition (sputtering) and surface segregation [33].
2. **Top-down:** Top-down methods involve reducing a larger structure until the desired nanoscale dimensions are obtained. In top-down methods, the van der Waals forces between the layers in bulk material are overcome, thereby separating the two dimensional sheets. Examples of top-down methods are mechanical (see Figure 2.9b) and liquid exfoliation [33].

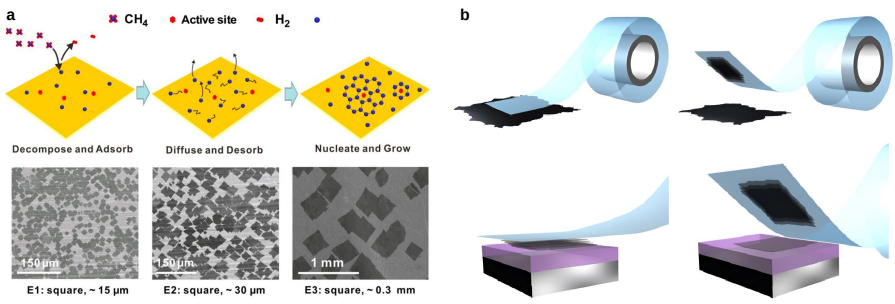

Figure 2.9: Two preparation methods of 2D materials: **(a)** The chemical vapor deposition (CVD) growth process of graphene on Cu. Figure adapted from [43]. **(b)** The mechanical exfoliation process using adhesive tape. Figure adapted from [44].

Among the most commonly used preparation methods of 2D monolayers are mechanical- and liquid exfoliation and, CVD. Mechanical exfoliation or mechanical cleavage, is a popular method to synthesize crystalline nanosheets because it simply involves peeling a piece of bulk material with Scotch tape and pressing it onto a targeted substrate as was first demonstrated with graphene in 2004 [45]. However, this method has low yield, and the nanosheets have a limited lateral size [33]. Liquid exfoliation is the preferred method for large scale production. It works through a liquid medium to effectively reduce the bond strength within a material compared to vacuum conditions. This makes it easier for external mechanical forces generated in processes like sonication, to break down the weak van der Waals forces between the layers. In the CVD method, one or more gas/vapor precursors are introduced into a chamber where the precursors are reacted and/or decomposed onto a substrate (e.g. copper) to grow high-quality thin films [33].

2.4. Characterization Techniques

The following characterization techniques enable us to extensively study 2D materials like h-BN to determine their structural and photophysical properties.

2.4.1. Optical Microscopy

In optical microscopy, a series of lenses is utilized to magnify images of relatively small samples (down to hundreds of nanometers), and there are various types of optical microscopes distinguished by their illumination method and approach to creating contrast in the magnified image.

1. **Illumination:** A wide-field microscope and confocal microscope illuminate the sample differently: wide-field microscopes illuminate the entire sample, whereas confocal microscopes employ two pinhole apertures to first illuminate a small sample area and then select light emitted from the targeted point offering higher resolution.
2. **Contrast:** Contrast in the magnified image can be produced through various methods. Bright-field microscopes illuminate the sample with white light and have two operating modes: transmission mode and reflection (epi) mode. In transmission mode, denoted by the blue optical path in Figure 2.10, the light transmitted by a transparent sample is collected and contrast is created by the absorption of light in dense areas of the specimen [46]. In reflection mode, denoted by the red optical path in Figure 2.10, light that is reflected by the surface of an opaque material re-enters the objective lens and contrast is generated based on variations in reflectivity across the sample.
3. **Fluorescence:** A fluorescence microscope employs light of a specific wavelength to illuminate the sample. If the sample contains fluorescent components like quantum emitters, and the excitation light is sufficiently energetic, these components can absorb and then release some of that energy as photons. A detector captures these photons, creating contrast based on variations in fluorescence across the sample.

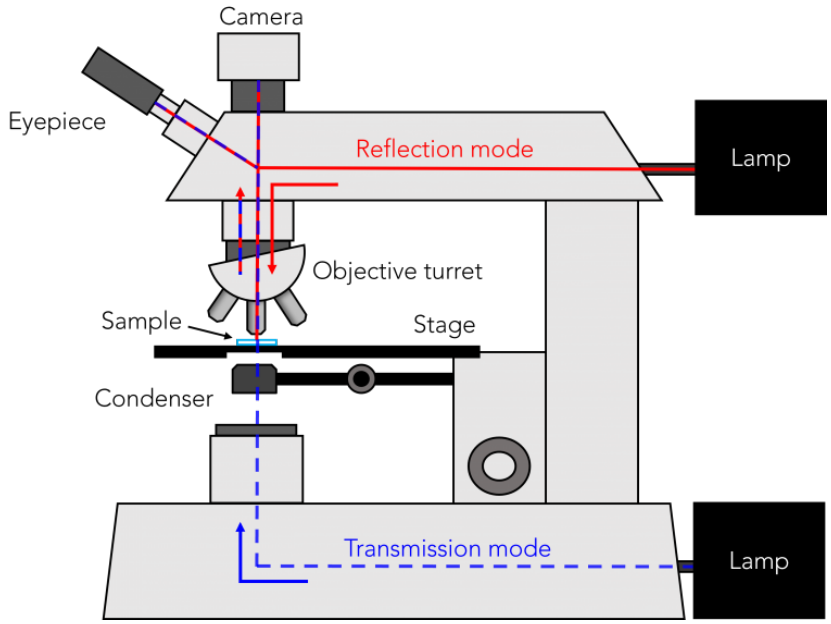

Figure 2.10: A schematic diagram of an upright microscope showing the optical paths for transmission mode (blue) and reflection mode (red). Figure adapted from [47].

2.4.2. Atomic Force Microscopy

Atomic Force Microscopy (AFM), a type of Scanning Probe Microscopy (SPM), is widely used for mapping surface topography with sub-nanometer precision. The technique is based on measuring atomic-scale forces between a sharp probe tip on a cantilever and the sample surface, which is measured using a laser directed at the back of the cantilever and a position-sensitive detector, as shown in Figure 2.11.

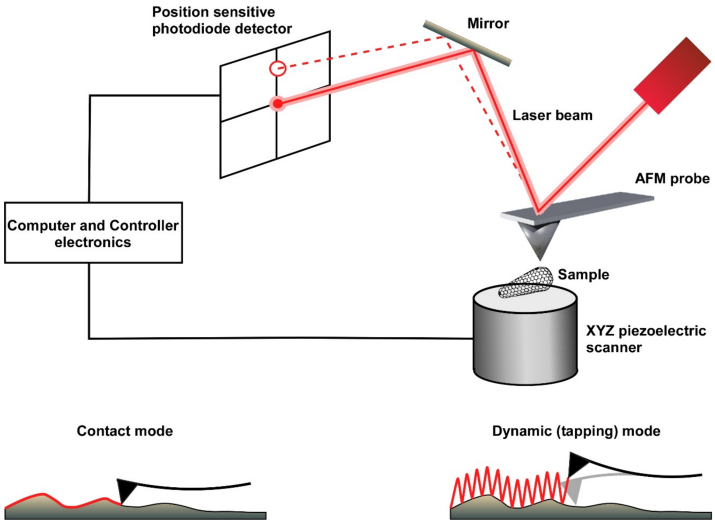

Figure 2.11: A schematic overview of the main components of an atomic force microscope (AFM) and its two operating modes: contact mode and non-contact (dynamic) mode. Figure adapted from [48].

At the interface between the tip and the sample, a complex interaction of short-range repulsive forces and long-range attractive forces occurs described by the highly nonlinear Lennard-Jones Potential in Equation 2.1. Here, r is the distance between two particles, ε quantifies their attractive strength, and σ is the separation distance between two particles at which the potential energy U is zero. The repulsive component, proportional to r^{-12} is a result of the mutual repulsion between the electron clouds of the tip and sample atoms. In contrast, the attractive component, proportional to r^{-6}, is due to van der Waals forces which is a result of dipole interaction between the tip and and sample.

$$U = 4\varepsilon((\frac{\sigma}{r})^6 - (\frac{\sigma}{r})^{12} \tag{2.1}$$

The two main AFM scanning modes, contact mode and tapping mode, operate within these regimes of interaction. Contact mode operates predominantly in the repulsive regime, while tapping mode transitions between the attractive and repulsive regimes. Below is a more detailed description of these two modes:

1. **Static mode:** In static mode (contact mode), the cantilever scans the sample while applying a constant force onto the surface of the sample. As the tip physically touches the sample, the cantilever will deflect proportional to the applied setpoint force. When the tip encounters a higher sample feature, the cantilever will bend and deflect more. This deflection will be projected by the laser onto the detector. A feedback loop responds by moving the Z scanner to restore the initial cantilever deflection and to keep the applied setpoint force constant. By tracking the displacement of the Z scanner, the surface topography of the sample can be determined.
2. **Dynamic mode:** In dynamic mode (tapping mode), the tip does not make physical contact with the sample, avoiding damage to both. When the tip approaches the sample surface, an attractive force arises between the atoms of the tip and sample. However, this force may not be strong enough to bend the cantilever. Therefore, the cantilever is oscillated close to its resonance frequency to detect this subtle force. As the tip moves closer to (away from) the sample, the attractive force increases (decreases), causing a decrease (increase) in the amplitude of the cantilever's oscillation. A feedback loop responds by moving the Z scanner to restore the oscillation amplitude to its set point. By tracking the displacement of the Z scanner, the surface topography of the sample can be determined.

2.4.3. Scanning Electronic Microscopy

Electron microscopy is a powerful imaging technique that has transformed our ability to observe micro- and nanoscale samples. Unlike traditional light microscopy, electron microscopy uses a focused beam of electrons to image the surface of a specimen. Since the wavelength of electrons is much smaller than that of visible light, much higher magnifications can be reached of about 100.000x. There are two main types of electron microscopy, namely scanning electron microscopy (SEM) and transmission electron microscopy (TEM). In this thesis, SEM is used.

In essence, SEM relies on the 'reflection' of a focused electron beam from the sample surface. When these high-energy electrons strike the sample, they undergo various scattering processes as shown in Figure 2.12a. The primary interactions include:

1. **Secondary electrons (SE):** These electrons are generated when the primary electron beam undergoes inelastic scattering, causing ionization and the subsequent ejection of electrons from the sample. The resulting image contrast is primarily influenced by the sample's surface topography, and the energy and incident angle of the electrons.
2. **Back scattered electrons (BSE):** These electrons result from the elastic scattering of the primary electron beam due to electrostatic interactions with the sample's atoms. The contrast in BSE images is determined by variations in the atomic number of the elements within the sample.

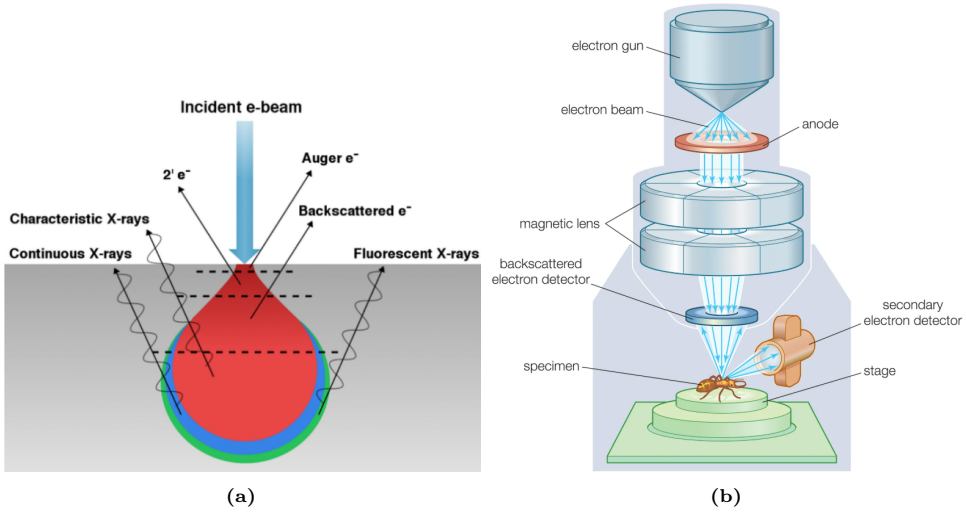

(a) (b)

Figure 2.12: (a) In scanning electron microscopy, scattering events produce various types of electrons including secondary electrons (2') and backscattered electrons. **(b)** Schematic of a scanning electron microscope. Figures adapted from [49] and [50].

When the number of electrons hitting the surface of the sample does not equal the number of electrons leaving the sample, the sample gets charged. This charging negatively affects the quality of the image, which is why it is advised to use electrically conducting samples or else to apply a thin conducting coating (e.g. gold) on non-conducting samples (such as h-BN).

Figure 2.12b shows the most important components of an SEM. Different types of detectors are used to detect the SEs and BSEs. Almost all SEs are collected and amplified by a scintillator-photomultiplier system. For the collection of BSEs, solid-state detectors are typically used.

2.4.4. Raman and Photoluminescence Spectroscopy

Spectroscopy is a useful technique for analyzing the chemical composition, structure, and molecular bonding of a sample, as well as for investigating fluorescent samples. By exciting a sample with a laser and measuring the energy of the scattered light, a spectrum can be collected. A spectrometer typically consists of a laser to excite the sample, a stage that holds the sample, a monochromator which disperses the scattered light into its constituent wavelengths, and a charged-coupled device (CCD) which collects the scattered light spectrum.

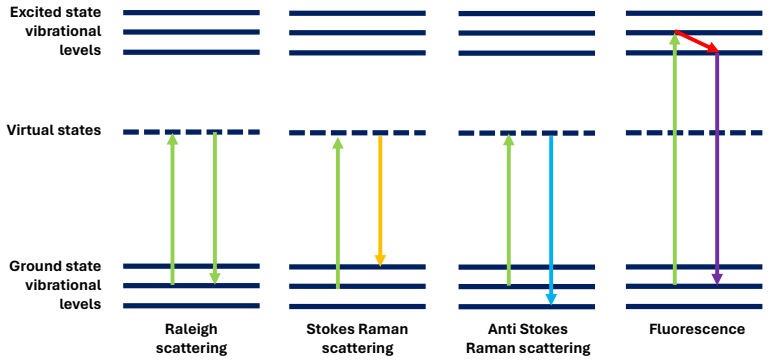

Figure 2.13: Energy diagram showing Raleigh and Raman scattering, and fluorescence. Figure adapted from [51].

Molecules and crystals exhibit distinct vibrational levels separated by discrete energy differences (2.13). When excited by a laser, excitation photons can undergo one of four processes: fluorescence (absorption and re-emission), transmission, elastic scattering (Rayleigh scattering), or inelastic scattering (Raman scattering). In both scattering processes, the photons excite the molecule from the ground state to a virtual state (dotted lines in the centre), which corresponds to the laser energy rather than a real energy level [52]. Most photons undergo Rayleigh scattering, maintaining their energy. In Raman scattering, however, photons return to higher (Stokes Raman) or lower (anti-Stokes Raman) vibrational levels of the ground state. Molecular vibration frequencies depend on molecular mass. Heavier molecules like oxygen (O_2) exhibit lower frequencies and longer wavelengths compared to lighter molecules like nitrogen (N_2). Complex molecules or crystals, such as h-BN, display multiple vibrational modes visible in the Raman spectrum. The Raman shift, representing the energy difference between incident and scattered photons, corresponds to the vibrational level differences and is independent of laser energy. Typically expressed in wavenumbers (cm^{-1}), the Raman shift is a key spectral feature. Figure 2.14 illustrates the Raman spectra of bulk h-BN.

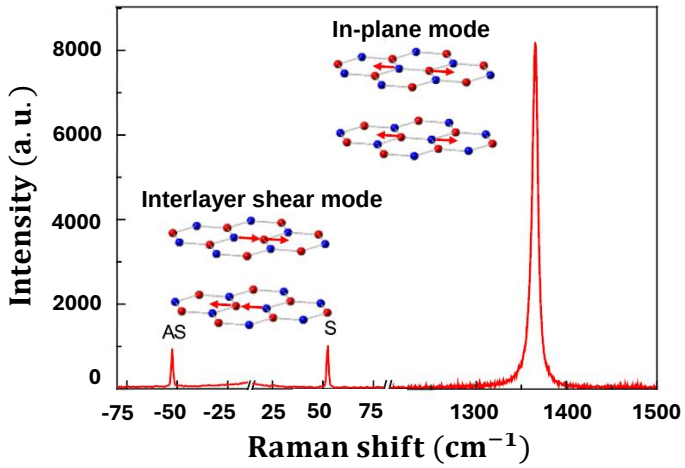

Figure 2.14: Raman peaks of the high frequency E_{2g} mode at 1366 cm^{-1} and low frequency E_{2g} mode at -52.5 cm^{-1} (Anti Stokes Raman) and 52.5 cm^{-1} (Stokes Raman) in bulk h-BN. Figure adapted from [53].

As explained in Section 2.1.1, if the excitation light is sufficiently energetic, the energy of the photons is sufficient to promote the molecule to an excited state (solid lines at the top of Figure 2.13). Fluorescent features in the sample can be excited and their emitted photons can be detected. These photoluminescence (PL) measurements are represented in the PL spectrum in terms of wavelengths (usually in nm), as shown in Figure 2.6.

Raman shift and strain

In h-BN, there are two E_{2g} vibration modes that exhibit Raman activity [54], as shown in Figure 2.14. One corresponds to a lower frequency mode, peaking at 52.5 cm^{-1} [53], while the other presents as a higher frequency mode, peaking at 1366 cm^{-1}. The high frequency mode involves in-plane vibrations where boron and nitrogen atoms oscillate in opposite directions, yielding a signal roughly 50 times more intense than the lower frequency counterpart [53][55]. This higher frequency mode is susceptible to factors such as strain, crystal deformations, defects, or temperature variations, offering a means to quantify strain within the crystal lattice [56][57].

In the case of compressive strain, the bond length between the atoms shortens, resulting in higher frequency vibrations of the lattice and thus a positive shift (to higher wavenumbers) of the E_{2g} Raman peak. While for tensile strain, the atomic bond lengths are lengthened, resulting in lower frequency vibrations of the lattice and thus a negative shift (to lower wavenumbers) of the E_{2g} Raman peak. This variation in the peak position can be related to the uniaxial strain according to Equation 2.2 [58]:

$$\Delta\omega = \Delta\omega^h \pm \frac{1}{2}\Delta\omega^s = -\omega^0\gamma(\varepsilon_{ll} + \varepsilon_{tt}) \pm \frac{1}{2}\beta\omega^0(\varepsilon_{ll} - \varepsilon_{tt}) \tag{2.2}$$

Where $\Delta\omega$ is the shift of the E_{2g} relative to zero strain, $\Delta\omega^h$ is the shift resulting from the hydrostatic component of the strain, $\Delta\omega^s$ is the mode splitting due to the shear component of the strain, ω^0 is the E_{2g} peak position at zero strain, γ is the Grüneisen parameter, β is the shear deformation potential in the lattice, and ε_{ll} (ε_{tt}) is a strain tensor component parallel (transverse) to the direction of strain.

Under biaxial strain, the shear deformation terms cancel (since ($\varepsilon_{ll} = \varepsilon_{tt}$) and the following relation can be found for the strain:

$$\varepsilon_{ll} = \varepsilon_{tt} = \varepsilon = \frac{-\Delta\omega}{2\gamma\omega^0} \tag{2.3}$$

Consequently, the E_{2g} mode is not expected to split under biaxial strain, whereas uniaxial strain does induce splitting. Figure 2.15 illustrates the splitting of the graphene G peak under uniaxial strain.

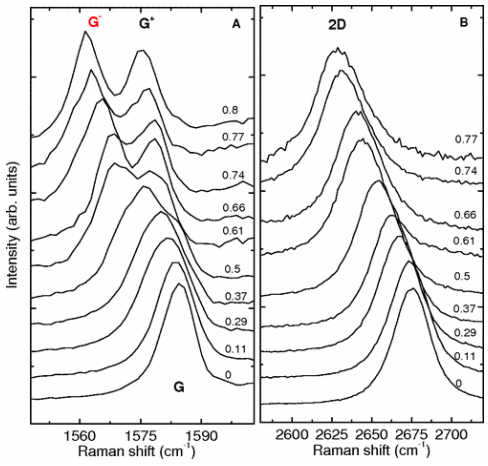

Figure 2.15: The G and 2D Raman peaks of graphene as a function of uniaxial strain. Figure adapted from [58].

3
State of the Art

To utilize quantum emitters in 2D materials as sensitive FRET-based nanoprobes for sequencing biomolecules, it is essential to gain control over their spatial and spectral properties. This chapter aims to provide an overview of the current state on quantum emitters in 2D materials and the methods to systematically engineer them.

3.1. Quantum Emitters in 2D Materials

This section outlines two of the most studied 2D materials as hosts for quantum emitters: TMDCs and h-BN.

3.1.1. Quantum Emitters in TMDCs

Quantum emitters in TMDCs were simultaneously reported in various papers in 2015 [59][60][61] at cryogenic temperatures. Subsequent research has been focused predominantly on two TMDCs - WSe2 and MoS2 - although emitters in WS2, GaSe, and MoSe2 have also been reported [17]. One of the suggested theories behind quantum emission in TMDCs is based on electron-hole pair (exciton) recombination. Generally, these excitons are not localized; however, they tend to drift towards lower energy regions such as crystallographic imperfections and potential wells before recombining (see Figure 3.1), which is also known as the funnel effect [62]. Lattice point defects such as missing atoms (vacancies) and interstitial atoms can serve as effective traps for excitons that enable quantum emission, and highly localized strain gradients can help to funnel the exciton.

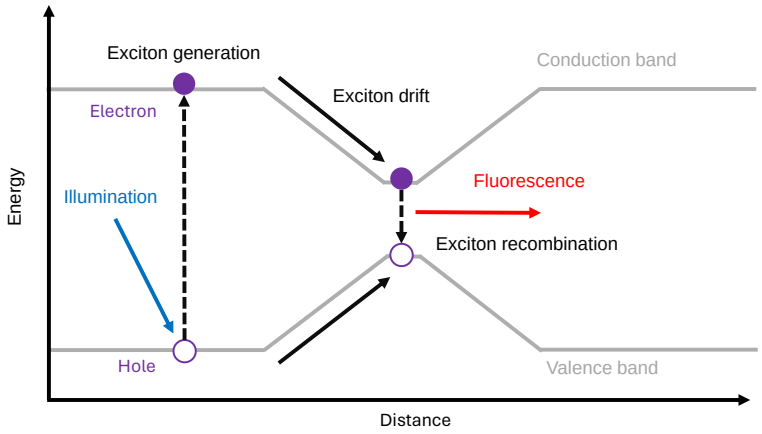

Figure 3.1: Diagram showing the funnel effect in TMDCs where the exciton drifts towards a lower energy region before it recombines. Figure adapted from [63].

3.1.2. Quantum Emitters in h-BN

For the first time in 2015, Tran et al. [4] demonstrated multi-color quantum emission in mono- and multilayer h-BN. They reported ultra bright, mostly optically stable quantum emission at room temperature.

The observed quantum emission can be attributed to colour centers, which are essentially wide band gap point defects. These atomic vacancies or impurities form intermediate energy levels lying between the conduction band and valence band. Electrons in the occupied energy states within the bandgap are excited to higher unoccupied levels, leading to spontaneous photon emission. A wide range of point defects in h-BN have been investigated including N_BV_N [4], carbon related defects [64] [65] [66], and oxygen related defects [67], covering the emission range from UV to near-infrared as is shown in Figure 3.2. Although there still remains a debate on the exact origins of quantum emission from defects in h-BN at specific wavelengths. Such defects can occur for example due to inclusion of contaminants during h-BN growth or in post-growth processes such as thermal annealing.

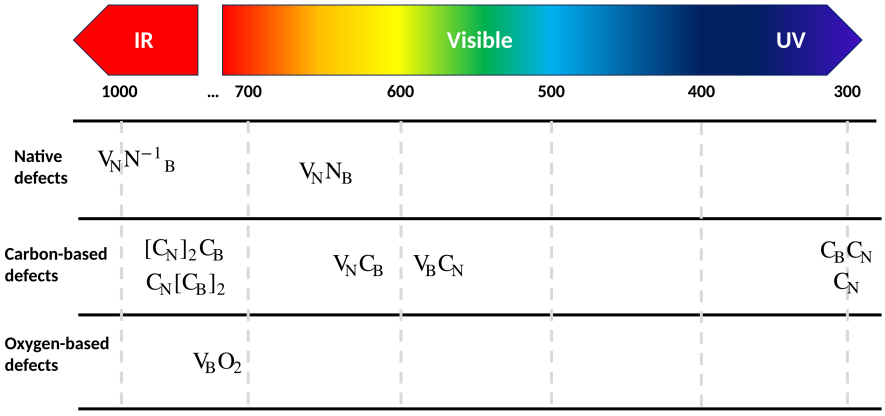

Figure 3.2: Emission range of various defects in 2D h-BN covering the near-infrared to UV.

3.1.3. Comparison

An overview of photophysical properties of quantum emitters in TMDCs and h-BN is given in Table 3.1. Noteworthy are the superior brightness and quantum yield of h-BN at room temperature.

Table 3.1: Photophysical properties of quantum emitters in different 2D materials (TMDCs and h-BN) [22].

Material	Operating temperature (K)	Emission wavelength range (nm)	Fluorescence lifetime (ns)	Brightness (kcps)	Quantum Yield (%)	Ref.
WSe_2	4	720-840	0.1, 0.3-225	3000	1, 60	[68] [69]
MoS_2	4	550, 660-730	< 0.15, 10.8	4	0.6, 95	[70]
h-BN	293	300-1000	1-3	7000	87 ± 7	[71]

3.2. Strain Engineering of 2D Materials and h-BN

As shown in Figure 3.3, strain-induced deformation of atomic defects in the crystal lattice of h- BN can distort the molecular orbitals and perturb its energy levels [72]. The remarkable mechanical strength of 2D materials offers the potential for substantial deformations, leading to significant electronic modifications [73]. Tuning the emission spectra of quantum emitters in h-BN could greatly increase the probability that multiple emitters have matching ZPL emission wavelengths [72] and by generating periodic strain fields, position-controlled quantum emitter arrays can be created. These advancements would significantly advance the realization of utilizing quantum emitters in 2D h-BN for FRET-based biosensing applications. This section discusses the state-of-the-art on various strain-induced deformation modes of 2D materials, with an emphasis on h-BN, that have been investigated theoretically, experimentally or both.

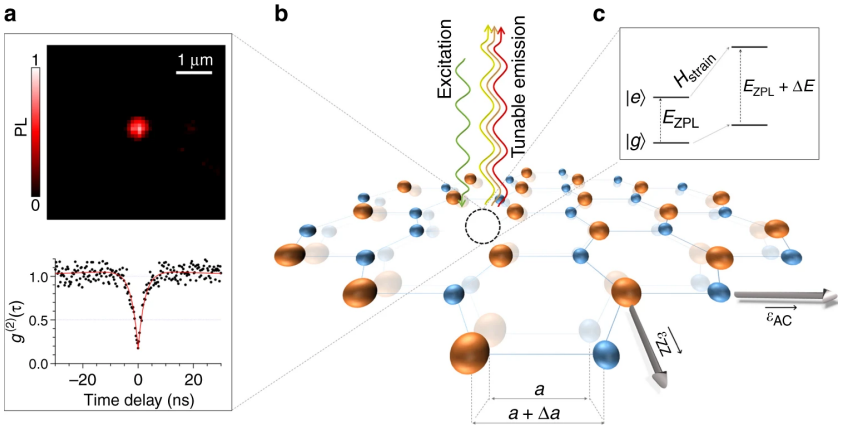

Figure 3.3: Tunable emission from atomic defects in hexagonal boron nitride at room temperature. **(a)** Top image shows the normalized intensity of emission for an isolated emitter. The bottom graph presents the second-correlation histogram of the quantum emission from the atomic defect, which is a measure of the time interval between two successive photons. **(b)** Here, the V_NN_B defect is schematically represented by a missing nitrogen atom (blue) and adjacent boron atom substituted by a nitrogen atom (orange). Tensile strain along the armchair (AC) and zigzag (ZZ) directions induce elongation Δa of the N-B bond length. **(c)** This deformation results in a shift of the energy levels of the atomic defect and allows tuning of the emission energy. Figure adapted from [72].

3.2.1. Stretching

Stretching involves elongating the substrate within its plane, with the relevant directions for h-BN being zigzag (ZZ) and armchair (AC), as depicted in Figure 3.3. The induced strain in the substrate is defined according to Equation 3.1, with the length of the substrate L. Accurately determining the strain transferred from the substrate to the sample poses a challenge. A large difference in Young's modulus between h-BN and the substrate decreases the efficiency of the strain transfer, making Equation 3.1 an upper limit of the strain in the flake.

$$\epsilon = \frac{\Delta L}{L} \cdot 100\% \tag{3.1}$$

Mendelson et al. [74] applied high degrees of intralayer tensile strain to quantum emitters in CVD-grown h-BN flakes on a polydimethylsiloxane (PDMS) substrate. The h-BN on PDMS assembly was mounted in a mechanical straining device (see Figure 3.4a) and optically characterized via confocal microscopy. They observed both blue and red spectral shifts in the defects with tuning magnitudes up to 65 meV for 5.55% strain applied to the PDMS substrate (see Figures 3.4e-f). This discrepancy in shifting direction was partially attributed to the possible variation in pre-existing strain between different defects. Overall trends in the strain-modified quantum emission are presented in Figures 3.4g-i.

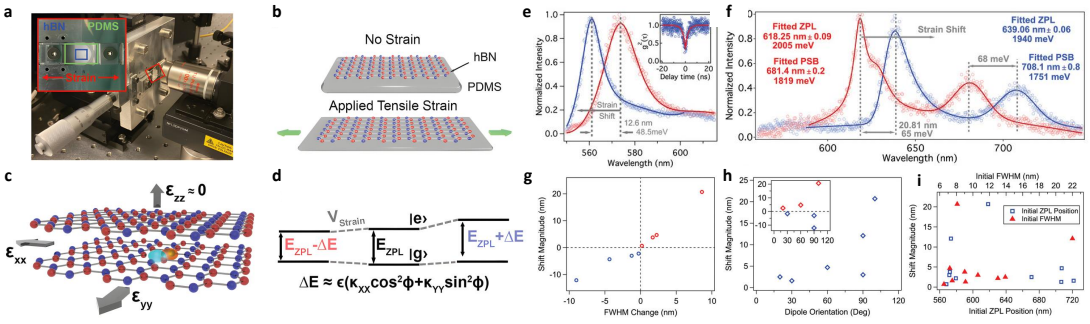

Figure 3.4: **(a)** The straining setup that was used to stretch the h-BN on PDMS assembly. **(b,c)** Schematics showing that intralayer tensile strain was applied. **(d)** Diagram depicting that upon the application of V_{strain}, the energy levels of the defect are modified, leading to an increased ZPL energy gain by ΔE. **(e,f)** Blue (65 meV) and red (48,5 meV) strain-induced spectral shifts. **(g-i)** Observed shift magnitudes plotted against: linewidth (FWHM) change, showing that blue shift narrows the linewidth and for red shift vice versa (g), dipole orientation of unstrained emitters, demonstrating larger shift magnitudes when the dipole orientation is more aligned with the applied strain field (along 90° axis) (h), and initial ZPL and FWHM position (0% strain), showing no clear dependence (g). Figures adapted from [74].

3.2.2. Bending

Bending refers to deformation of the substrate whereby it curves or flexes. The induced strain in the substrate is defined according to Equation 3.2 and Figure 3.5, with beam thickness h, distance from clamp to flake d, distance from clamp to deflection point L, and beam deflection δ.

$$\epsilon = \frac{3h\delta(L-d)}{2L^3} \tag{3.2}$$

Grosso et al. [72] applied bending-induced strain on ion irradiated and subsequently annealed quantum emitters in h-BN flakes. The h-BN flakes were deposited onto a flexible polycarbonate (PC) beam which was subjected to bending, resulting in both tensile strain (x-direction) and compressive strain (y-direction) due to the Poisson's ratio of 0.37 for PC (see Figure 3.5a). As depicted in Figure 3.5b, they found an extrapolated ZPL tuning range of -3.1 to 6 meV per percentage of strain applied to the substrate. This variability in shifting direction was also attributed to the initial conditions of the emitters such as pre-existing strain and lattice mismatches caused by sample fabrication.

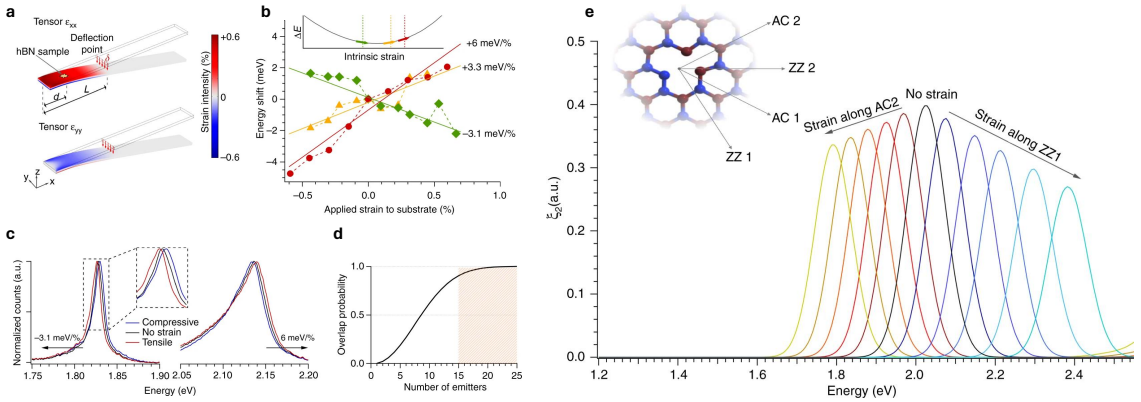

Figure 3.5: **(a)** Illustration showing the h-BN flake on a polycarbonate (PC) beam that is subjected to a vertical displacement δ at distance L from the clamping point. **(b)** The scaled energy shift as a function of applied strain to the bendable substrate for three emitters with different tunability of -3.1 meV/% (green), $+3.3$ meV/% (yellow) and $+6$ meV/% (red). The difference relates to the initial strain conditions of the emitters before the experiments. **(c)** The spectra of the emitters exhibit tunability ranging from -3.1 meV/% to 6 meV/% for compressive (blue), tensile (red), and no strain (black). **(d)**The probability of spectral overlap between two of n emitters increases as more emitters are added, reaching over 90% when at least 15 emitters with random ZPL energies are present, considering a 6 meV tuning limit and a ZPL spectral distribution of 300 meV. **(e)** Simulated optical response in the form of the imaginary part of the dielectric function ξ_2 as a function of strain (1-5%) in two different directions w.r.t. the N_BV_N defect. Figures adapted from [72].

Interestingly, they noted that for a maximum tuning range of 6 meV, two random emitters can be spectrally matched with a probability of $P > 0.9$ when there are at least 15 emitters present (see Figure 3.5d). Additionally, density functional theory (DFT) simulations were performed to investigate the effect of strain along different crystallographic directions on the energy shift in the N_BV_N defect (see Figure 3.5e).

3.2.3. Nanopatterns

This method utilizes the conformal deformation of 2D materials to the surface topography of a 3D patterned substrate, due to van der Waals forces, to induce local strain. While nanopatterned substrates enable localized strain, it often lacks mechanical reconfigurability due to its rigid structure. Two examples of different 3D patterned substrates are: Pillars and Spheres.

Pillars - Proscia et al. [75] showcased an example of employing a patterned substrate through nanopillars (see Figure 3.6a-b) to optically activate an array of point defects in CVD-grown h-BN flakes. From confocal PL measurements, they observed selective emission from the pillar sites, demonstrating near-deterministic activation of quantum emitters. An average brightness contrast of ∼100 was reported between pillar sites versus inter-pillar sites and a relatively narrow emission wavelength distribution with a peak around 540 nm (see Figure 3.6c). Interestingly, through assessing the light emission

intensity across various topologies such as circular or triangular pillars, they suggested that all defects become luminescent under optical excitation when a minimum strain threshold is reached. However, the strain on these pillar sites was not quantified.

Spheres - Chen et al. [76] transferred an exfoliated multilayer h-BN flake onto hexagonal close-packed silica spheres on a silica substrate to induce local strain fluctuations. They compared PL and Raman spectra of both strained and unstrained regions and quantified the induced tensile strain to be 0.1% at the apex of the sphere, resulting in 40 meV blue shifts of the ZPL wavelength. The results from the PL measurements show that, regardless of the excitation power, the defects in the unstrained region showed no activity whereas the photon emission intensity in strained regions increases linearly with the excitation power, indicating that strain can activate defects in h-BN crystals.

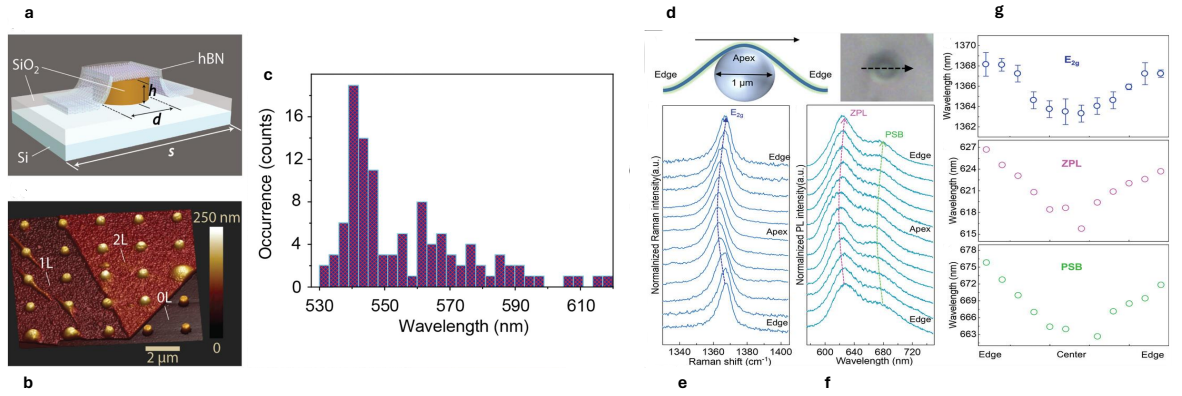

Figure 3.6: **(a)** SiO_2 pillar with h-BN flake on top. **(b)** AFM image of the nanopattern with indicated layer thickness of the h-BN. **(c)** The average peak wavelengths of emitters on an 8x10 array of 75 nm diameter pillars was found to predominantly concentrate around ∼540 nm. Figures adapted from [75]. **(d-f)** Line-scanning Raman and PL measurements of a strained hBN flake over a single micro-sphere. The black arrow indicates the scanning direction. **(e)** Position (strain) dependent E_{2g} high peak, ZPL, and PSB extracted from (e-f). Figures adapted from [77].

3.2.4. Wrinkles

Wrinkles are out of plane deformations like buckles and ripples which form in 2D materials due to partial strain relaxation. The maximum uniaxial tensile strain ϵ is accumulated on top of the wrinkles and can be estimated by Equation 3.3 [63], with Poisson's ratio v, flake thickness h, wrinkle width δ and wrinkle height λ. Below, thermal annealing and buckling-induced delamination for creating wrinkles in atomically thin crystals are described, where the latter has thus far only been documented for TMDCs.

$$\epsilon = \frac{\pi^2 h \delta}{(1 - v^2)\lambda^2} \tag{3.3}$$

Thermal Annealing - One method to (intentionally) create wrinkles is thermal annealing in which the difference in or even opposite polarity of the thermal expansion coefficients of h-BN and the substrate is utilized. Oliveira et al. [78] demonstrated that thermally annealed 2D h-BN samples on Si/SiO_2 tend to wrinkle along the armchair direction. As presented in Figures 3.7a-b, the wrinkles formed networks of threefold and occasionally fourfold origami-type junctions. Similar results from Chen et al. [79] supported these findings. They additionally tried different substrates and observed that the density of wrinkles on a sapphire (Al_2O_3) substrate was relatively high compared to quartz, silicon, and silicon carbide, as shown in Figure 3.7c. This likely involves the higher thermal expansion coefficient of sapphire compared to the other substrates. Furthermore, the wrinkle density was found to increase for decreasing flake thickness on a sapphire substrate.

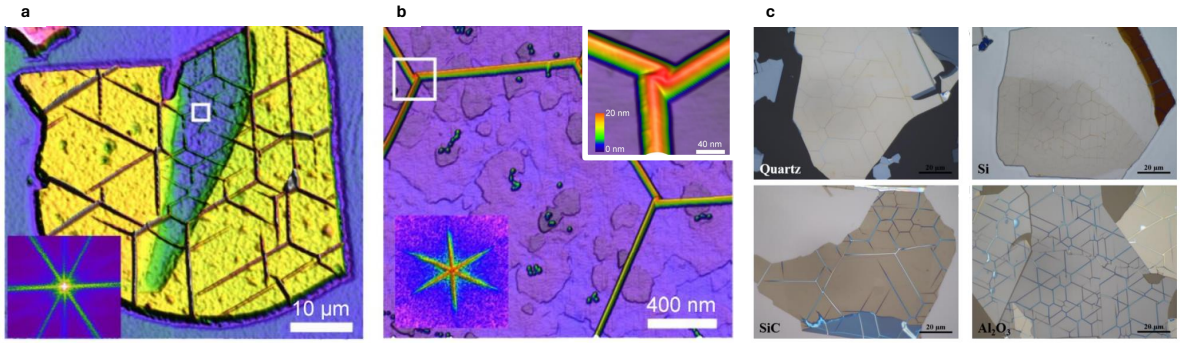

Figure 3.7: **(a,b)** Characterization of wrinkled h-BN flakes post-annealing using AFM. The bottom-left inset shows the FFT image of the flake topography. Figures obtained from [78]. **(c)** Optical microscopy image of wrinkles in h-BN flakes of similar thickness on varying substrates after annealing. The highest wrinkle density was observed on a sapphire substrate. Figure adapted from [79].

The effect of wrinkles in exfoliated and annealed h-BN on the formation of defect centers was experimentally and theoretically studied by Yim et al. [80]. By combining optical microscopy and PL measurements, they observed that the density of emitters on wrinkles far exceeded the density of emitters found on the flat plane (see Figures 3.8d-e). Additionally, the energy distribution of emitters located on the wrinkles was centered around wavelengths of 575 nm and 660 nm, suggesting the presence of distinct defects whereas emitters on the flat surface are more evenly distributed over a wider spectral range. Furthermore, the symmetry axis of the defects was found to align with the wrinkle direction, showing a correlation between the polarization direction of the emitter and the wrinkle direction as shown in Figures 3.8b-c. Using the results from density functional theory in Figures 3.8f-k, they showed that the large curvature of a wrinkle is energetically favorable especially to vacancy-based defects (e.g. $V_N N_B$ and $V_N C_B$) due to a dimerization of their dangling bonds. This lowers the defect formation energy, resulting in a curvature-induced large energy gain on the order of electronvolts. However, no experimental study was conducted to relate the strain in the wrinkles to the emission energy of defects in h-BN.

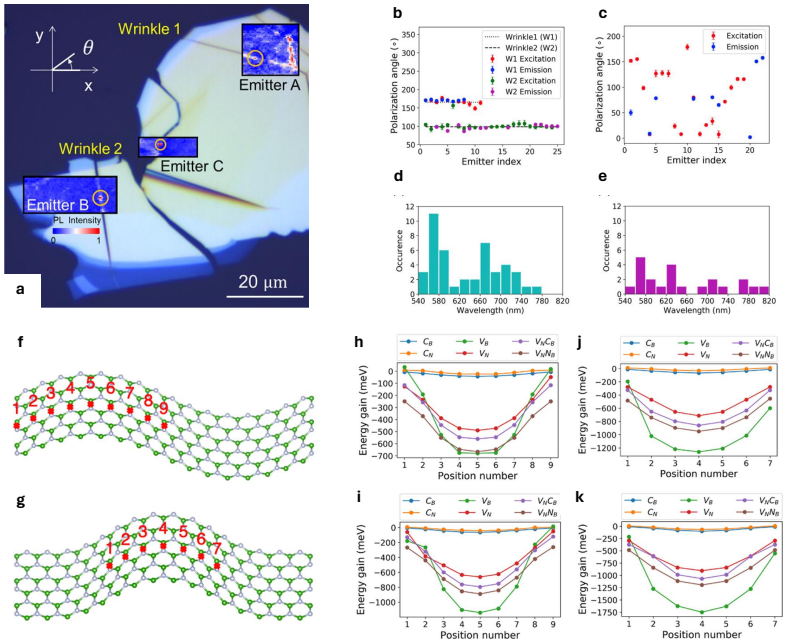

Figure 3.8: **(a)** Optical microscopy image of the wrinkled h-BN flake overlapped by the confocal PL map. Emitters A and B are on a wrinkle whereas emitter C is on a flat surface. **(b)** Excitation and emission polarization angle θ_0 of the emitters formed on wrinkle 1 (W1) and wrinkle 2 (W2). The angle of W1 and W2 are indicated by the short and long dashed lines, respectively. **(c)** Excitation and emission polarization angle θ_0 of the emitters formed on a flat surface. **(d)** Histogram of the peak wavelength of the emitters formed on wrinkles. **(e)** Histogram of the peak wavelength of the emitters formed on a flat surface. **(f,g)** Sine-shaped and Gaussian-shaped h-BN supercells used for simulations of defects in the presence of a wrinkle. The red asterisks denote possible defect sites across the wrinkle. **(h, j)** Curvature-driven energy gain of various defects as a function of the position across the sine-shaped wrinkle with two different curvatures: 0.75 and 1.05 nm^{-1}, respectively. **i, k)** Curvature-driven energy gain of various defects as a function of the position across the Gaussian-shaped wrinkle with two different curvatures: 1.08 and 1.58 nm^{-1}, respectively. Figures adapted from [80].

Buckling-induced delamination - This method involves depositing a 2D material on a pre-stretched elastomeric substrate after which the tension is suddenly released to create the wrinkles (see Figure 3.9a). Castellanos-Gomez et al. [63] created large local strains of up to 2.5% in 3-5 layer MoS_2, as single and bilayer samples were found to be unstable and tended to collapse upon folding. The applied strain was quantified by a combination of AFM and Raman spectroscopy, and the effect on the bandgap was analyzed by scanning photoluminescence. They observed that the uniaxial strain on top of the wrinkles reduced the energy of the direct bandgap transition by 90 meV (see Figure 3.9d-e), forming a trap for excitons. Similarly, Yang et al. [81] were able to generate wrinkles in $ReSe_2$, another TMDC. They controlled the morphology of the wrinkles by varying the flake thickness, where fewer layers resulted in sharper wrinkles (see Figures 3.9f-h). Furthermore, they observed that different pre-strains affect the amplitude and periodicity of the wrinkles, with a small pre-strain of 30% resulting in the collapse of wrinkles. The local strain on top of a monolayer wrinkle in Figure 3.9i was estimated to be 1.64% using Equation 3.3, resulting in a direct bandgap red shift of 70 meV.

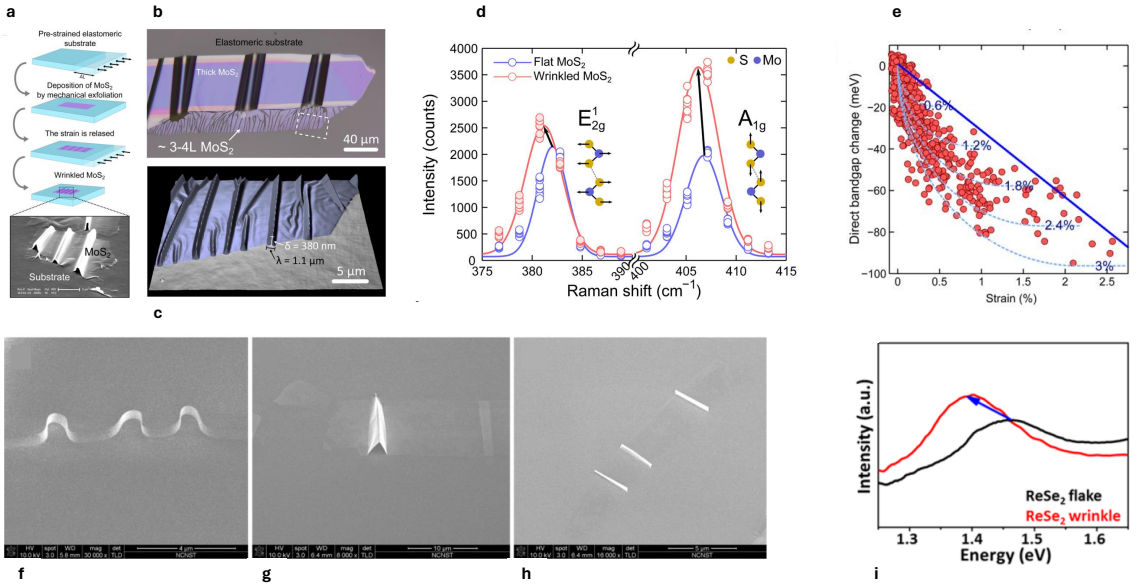

Figure 3.9: **(a)** Schematic representation of the buckling-induced delamination process to fabricate wrinkles in few-layer MoS_2. **(b,c)** Optical microscopy and AFM images of the wrinkled MoS_2, respectively. **(d)** Raman spectra measured on a flat (blue) and on a wrinkled (red) region of a 4-layer-thick MoS_2 flake. The E_{2g} mode shows the largest shift to the left. **(e)** The direct bandgap transition energy plotted against the strain measured by scanning the laser across more than 50 wrinkles. The dashed lines show the expected bandgap vs strain relationship after accounting for the effect of the finite laser spot size and the funnel effect. Figures adapted from [63]. **(f-h)** SEM images of different wrinkle morphologies of $ReSe_2$ with varying thickness: ripple for multilayer flakes (f), triangle for few-layer flakes, and needle for monolayer flakes (h). **(i)** PL measurement on flat (black) and wrinkled (red) regions in the same position of the $ReSe_2$ monolayer. Figures adapted from [81].

The aforementioned strain engineering techniques have been summarized in Table 3.2. Noteworthy is the lack of empirical data on the reversibility of wrinkles in 2D h-BN and the energy shift that could be achieved.

Table 3.2: Summary of experimental results from strain engineering quantum emitters in literature.

Wrinkles					
Authors	Method	Localized	Reversible	Strain (%)	Energy shift (meV)
Oliveira et al. [78]	Annealing	Yes	Unknown	Unknown	Unknown
Yim et al. [80]	Exfoliation	Yes	Unknown	Unknown	Unknown
Castellanos-Gomez et al. [63]	Buckling	Yes	Yes	2.5	90
Yang et al. [81]	Buckling	Yes	Yes	1.64	70
Miscellaneous					
Authors	Method	Localized	Reversible	Strain (%)	Energy shift (meV)
Mendelson et al. [74]	Stretching	No	Yes	5.55[1]	65
Grosso et al. [72]	Bending	No	Yes	1[2]	-3.1, 6
Proscia et al. [75]	Pillars	Yes	No	Unknown	Unknown
Chen et al. [77]	Spheres	Yes	No	0.11-0.15	39

[1]Strain applied to the substrate.
[2]Strain applied to the substrate.

4
Research Proposal

This chapter will present the research proposal by formulating the knowledge gap and research questions.

4.1. Knowledge Gap

Until now, no systematic approach has been reported in literature that achieves photostable, localized, and spectrally uniform quantum emitters in 2D h-BN simultaneously. Wrinkling to achieve this goal has not been widely investigated in literature yet. Thus far, the formation of wrinkles under high temperature annealing conditions has been reported [84] and methods have been developed to quantify the induced strain in the wrinkles [55]. Furthermore, a decrease in formation energy of vacancy-based defects has been found to correlate with the curvature of wrinkles in h-BN flakes [86]. However, no experimental research has been conducted that systematically studies the structural properties of wrinkles in 2D h-BN and correlates these properties to the photophysical properties of quantum emitters. Moreover, utilizing wrinkles in 2D h-BN for optofluidic applications, such as single-molecule fingerprinting, presents a novel research direction. As such, it is unclear under what conditions this could be achieved. Therefore, it is important to gain a comprehensive understanding of the wrinkling behaviour of 2D h-BN and to relate key mechanical properties (such as spatial distribution, morphology, and strain) to the photophysical characteristics of quantum emitters (including spatial distribution, emission energy, and photostability). Additionally, exploring how these properties are influenced in an optofluidic context remains an open question.

4.2. Research Questions

From the knowledge gap, a main research question and three sub-questions, which will be quantitatively researched, have been formulated:

1. What are the characteristic structural properties of wrinkles in 2D h-BN flakes, and how do these features relate to the photophysical properties of quantum emitters in the context of optofluidic applications?

    (a) What are the detailed structural properties of wrinkles in 2D h-BN flakes, and how are these features influenced by the substrate material?

    (b) What are the photophysical properties of quantum emitters in 2D h-BN flakes and how do these relate to the identified structural properties of the wrinkles?

    (c) How does the presence of liquid affect the structural properties of wrinkles in 2D h-BN flakes and the corresponding photophysical properties of quantum emitters?

5 Methodology

Having identified the knowledge gap and formulated the research questions and objectives in chapter 4, this chapter will outline the various methods and techniques used to prepare, fabricate, and characterize the samples. This plan will serve as a framework for a quantitative experimental study to address the research questions effectively.

5.1. Sample Preparation

Proper sample preparation is an important process to ensure contamination-free substrates and good adhesion of h-BN flakes, consisting of two main steps:

1. **Substrate cleaning** - Substrates are initially cleaned in acetone and subsequently in isopropylalcohol (IPA) in an ultrasound sonicator for 3 minutes to remove oils and organic contaminants from the surface. Following this, the substrates undergo treatment with 100W oxygen plasma at low pressure for 5-10 minutes to get rid of all residual organic contaminants and enhance the surface energy, thereby improving the adhesion of the h-BN flakes.
2. **h-BN exfoliation and transfer** - As discussed in Section 2.3, h-BN consists of layers that are interconnected by relatively weak van der Waals forces, in contrast to the stronger inter layer covalent bonds. These van der Waals forces can be overcome by applying a mechanical force to the bulk h-BN crystal using adhesive tape. Exfoliated layers from the crystal are transferred to another tape and peeled off again, resulting in progressively thinner layers. This process is repeated multiple times until the flakes reach a desired thickness, usually ranging from a few to several hundreds of nanometers.

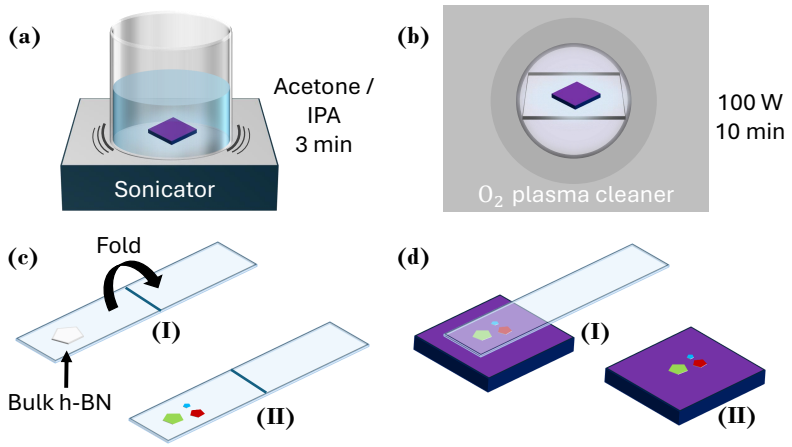

Figure 5.1: Schematic of the sample preparation process with Si/SiO_2 substrate in purple. **(a)** Sonication in acetone and isopropylalcohol (IPA) for 3 mins each. **(b)** Oxygen plasma cleaning was done in a Diener plasma etcher at 100 W for 10 minutes. **(c)** Flake exfoliation process using Scotch-tape: (I) Bulk h-BN crystal on a zero tape (II) By folding the zero tape on itself, the h-BN crystal is broken down into smaller flakes distributed over a larger area. New tapes can be used to exfoliate flakes from the zero tape until the desired flake distribution is reached. **(d)** With the direct transfer method, the tape is directly pressed onto the substrate.

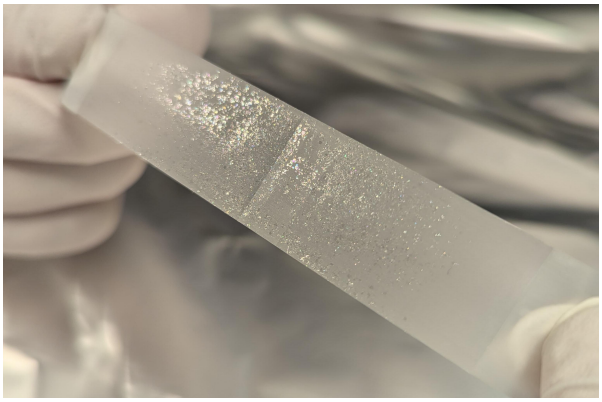

Figure 5.2: Exfoliation tape containing an even distribution of h-BN flakes.

Once the exfoliation tape has reached a sufficient concentration of flakes as shown in Figure 5.2, it is pressed onto the cleaned substrate and then peeled off, leaving behind a variety of hBN flakes as shown in Figure 5.3. The colour of a flake serves as a qualitative indicator of its thickness [82]. This effect results from optical interference; as light reflects off the different interfaces of the flake and substrate, variations in the light path length cause constructive or destructive interference. These interference patterns produce observable colour shifts that correlate with the flake's thickness.

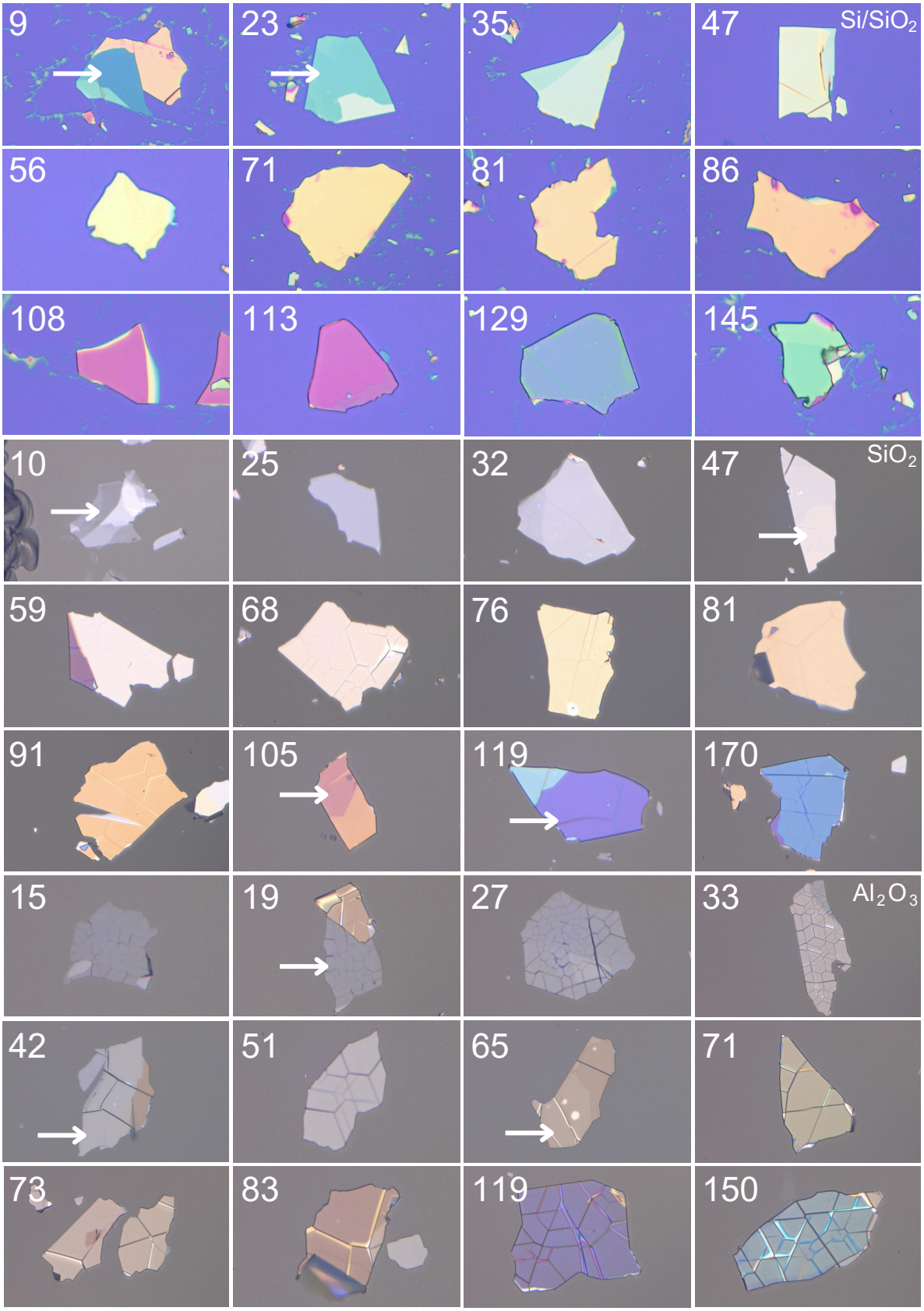

Figure 5.3: Thickness- and substrate-dependent colour of h-BN on Si/SiO_2, quartz (SiO_2), and sapphire (Al_2O_3).The figure shows a mix of pre- and post-annealed flakes, explaining the variations in wrinkle density. The flake thickness (in nanometers) is indicated in the top left corner, with arrows pointing to the relevant regions when multiple thicknesses are present. Images were captured using the Keyence VHX-6000 microscope with combined coaxial lighting and a brightness setting of 50. Flake thickness was determined with AFM.

5.2. High Temperature Annealing

High temperature annealing is chosen as the primary method for generating wrinkles in the h-BN flakes. As outlined in Section 3.3.4, wrinkles may arise during the annealing process as a result of opposite polarity in thermal expansion coefficients between the substrate and h-BN. This process is illustrated in Figure 5.4.

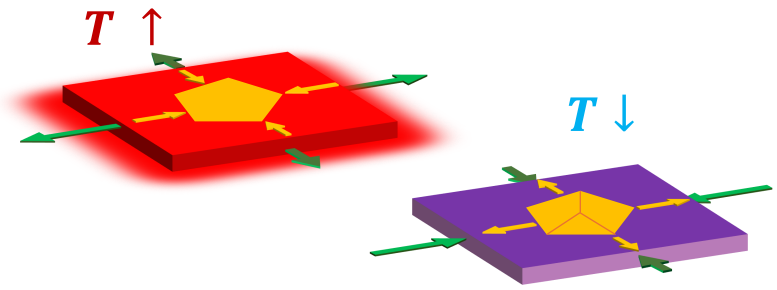

Figure 5.4: Schematic representation of wrinkle formation in h-BN flakes during the thermal annealing process. The arrows indicate the straining directions of the substrate (green) and h-BN (yellow).

When heated, the substrate, typically with a positive in-plane thermal expansion coefficient (TEC), expands, while the h-BN, having a negative in-plane TEC, contracts, subjecting the h-BN to tensile strain. During the cooling phase, this process reverses, resulting in compressive strain on the h-BN. The thermally induced strain can be quantified by Equation 5.1, where α_s is the TEC of the substrate, α_f is the TEC of h-BN, T_1 is the starting temperature, and T_2 is the annealing temperature. Once the in-plane compressive strain reaches a critical threshold, wrinkles form to partially relieve this strain.

$$\Delta\varepsilon_{th} = \int_{T_1}^{T_2} (\alpha_s - \alpha_f)\delta T \tag{5.1}$$

Table 5.1 presents the TEC values of h-BN and the substrates used in this report. The SiO_2 layer on top of the silicon is a 285 nm thick, lab-grown film, while the quartz refers to fused silica, explaining the slight difference in their TEC values.

Table 5.1: In-plane thermal expansion coefficient of h-BN and substrates used in this report.

Substrate	Thermal Expansion Coefficient (K^{-1})
h-BN	-2.9×10^{-6} [83]
Si	2.5×10^{-6} [84]
SiO_2	5.6×10^{-7} [85]
Quartz	5.5×10^{-7} [86]
Sapphire	5.0×10^{-6} [87]

Additionally, thermal annealing has been shown to both activate emitters in h-BN and stabilize those that exhibit blinking behaviour [88].

5.2.1. Annealing Parameters

The annealing parameters that were considered in this study are:

1. **Environment:** Annealing was predominantly done in high vacuum. However, one study reported that ion-irradiated samples annealed in vacuum produced less stable emitters compared to those annealed in argon [88], although the vacuum pressure was not specified. If similar results were observed in this study, annealing in argon could be reconsidered.
2. **Temperature:** One study found that stable emitter formation increases with annealing temperatures from 200–1200 °C [79], while another reported an optimal range of 800–850 °C due to

excessive defect diffusion inside the flake at higher temperatures [89]. Thus, 1000 °C was chosen to balance defect diffusion and maximizing wrinkle formation, as the maximum compressive strain depends on the annealing temperature.

3. **Duration:** There seems to be no standardized approach to annealing time in literature, with reported times ranging from 30 minutes to 4 hours and only one study noting excessive defect diffusion for prolonged durations. In this study, an annealing time of 2 hours (excluding heating up and cooling down) was used.

5.2.2. Tube Furnace Setup

Annealing is performed in a quartz tube furnace, capable of operating at temperatures up to 1100 °C under various gaseous environments, including argon, air, and vacuum. Figure 5.5 shows an overview of the setup and its components. The furnace is equipped with a thermocouple for temperature monitoring and a mass flow controller to regulate gas flow rates. For the annealing process, samples are placed in an alumina annealing boat positioned in the center of the heater to ensure uniform heating.

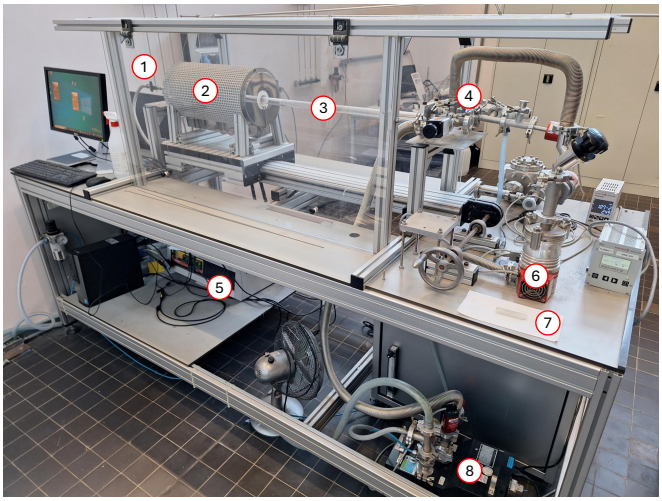

Figure 5.5: The quartz tube annealing setup in the deposition lab at the faculty of mechanical engineering. **(1)** Gas inlet valve **(2)** Heater **(3)** Quartz tube **(4)** Tube entrance **(5)** Heater controller **(6)** High vacuum pump **(7)** Alumina annealing boat **(8)** Low vacuum pump.

Figures 5.6a and 5.6b illustrate the temperature profiles of the annealing furnace during the heating up and cooling down phases. The samples are heated to 1000 °C and held at this temperature for 2 hours before the heater is turned off, allowing the furnace to cool naturally to room temperature.

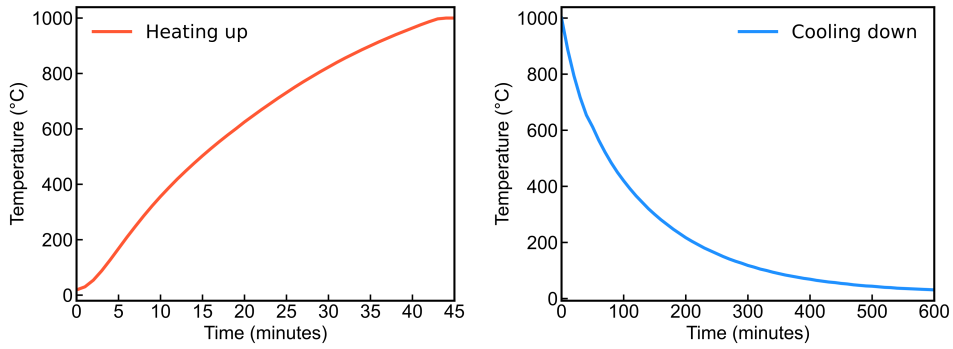

(a) **(b)**

Figure 5.6: Temperature profile of the annealing cycle showing the progression from room temperature to 1000 °C during heating up **(a)** and the subsequent cooling back to room temperature **(b)**. In between heating up and cooling down, the temperature is kept constant at 1000°C for 2 hours. Data acquired by taking a time-lapse of the heater readout.

5.3. Characterization

This section discusses all methods and instruments used to characterize the photophysical and structural properties of quantum emitters and wrinkled h-BN, presented in the order of their application: Optical microscopy, Raman and photoluminescence spectroscopy, Atomic force microscopy, and Scanning Electron Microscopy.

5.3.1. Optical Microscopy

Bright-field Microscopy - Bright-field images were taken as a preliminary step to examine the shape and thickness of flakes both before and after annealing. The Keyence VHX-6000 digital microscope, a widefield microscope capable of operating in both bright-field and dark-field modes, was used for this purpose. This microscope is equipped with two lenses and offers magnification of up to 2000x. Additionally, its built-in camera was used to photograph the samples.

Fluorescence Microscopy - Epi-fluorescence measurements were conducted to localize quantum emitters in the sample. These measurements were performed using the Nikon Eclipse Ti2 inverted epi-fluorescence microscope, equipped with a Teledyne Prime BSI Express sCMOS image sensor. A 60x water immersion objective lens was used for all experiments. The system's 488 nm, 532 nm, and 635 nm lasers, combined with bandpass filters, were used to localize quantum emitters with different excitation energies within this range. For each measurement, a time series was captured with an exposure time of 100 ms, 100% laser power (50W for 532 nm and 10.6W for 488nm), over a period of 40 seconds with no delay between frames. These time series were processed using ImageJ [90] to process stacked images and intensity profiles.

5.3.2. Raman and Photoluminescence Spectroscopy

Raman Microscope Systems - Raman and photoluminescence spectra were acquired using the Renishaw inVia Raman microscope to investigate the strain distribution, orientation of wrinkles, and the emission energies of quantum emitters. Two of these systems were employed for this study: one located at the Kavli Nanolab and the other at the Faculty of Aerospace Engineering. These systems offered slightly different configurations. The Kavli system featured 514 nm and 488 nm lasers paired with 1800 mm^{-1} and 3000 mm^{-1} gratings, respectively. The Aerospace Engineering system included 532 nm and 785 nm lasers with 1800 mm^{-1} and 1200 mm^{-1} gratings, respectively.

Laser Configurations - For photoluminescence spectra, the 514 nm was laser used with an 1800 mm^{-1} grating, providing a broad spectral range of 550–670 nm. Raman spectra were acquired using the 488 nm laser in combination with a 3000 mm^{-1} grating. This finer grating offers higher spectral resolution, essential for detecting small shifts in the E_{2g} Raman peak positions. The narrower spectral range of the finer grating is suitable here, as the focus is limited to the region around the peak. For all measurements, a 100x objective was used.

StreamHR - For Raman mapping, the built-in StreamHR function was used, which simultaneously performs sample movement, data collection, and readout, making it much faster than conventional mapping which takes these steps in sequential steps [91]. However, this function was not applied to PL mapping due to its limited spectral range and exposure time.

Polarization and Interference - The laser systems also differed in polarization. The Kavli lasers were circularly polarized and used for general mapping tasks, while the Aerospace Engineering lasers were linearly polarized, making them useful for correlating wrinkle orientation with the crystallographic directions of h-BN. To minimize quenching of the quantum emitters by the laser, photoluminescence spectra were recorded before Raman mapping. Raman spectroscopy targets vibrational energy levels, which are less affected by laser exposure as long as the sample does not overheat. In fact, quenching of the emitters can benefit Raman measurements by reducing fluorescence interference in the spectrum.

5.3.3. Atomic Force Microscopy

AFM imaging was performed to study the topography and morphology of the samples. The measurements were conducted using the Nanosurf Nanite B AFM, which is capable of operating in both dynamic and static mode. Dynamic mode was primarily used, as it minimizes sample damage and reduces tip wear by limiting direct contact with the surface. Additionally, dynamic mode is less susceptible to overshoot when the tip encounters highly elevated wrinkles or delaminated flake edges. The tips used were of the type NCLR-10 and had a stiffness of 48 Nm^{-1}. Static mode was employed when the resolution of the dynamic mode images was found to be insufficient. While this mode involves constant tip-sample contact, which can lead to increased tip wear and potential sample damage, it remains useful for measuring the tiniest features. The tips used were of the type CONTR-50 and had a stiffness of 0.2 Nm^{-1}.

5.3.4. Scanning Electron Microscopy

Two scanning electron microscopes were utilized—the FEI Nova Nano SEM and FEI Helios G4 CX—which are both at the Kavli Nanolab. The use of two different systems was based solely on equipment accessibility rather than a technical reason. An accelerating voltage between 5-10 kV was used and the samples on sapphire were gold coated resulting in slightly sharper images.

6
Results and Discussion

6.1. Characterization of Wrinkles

The structural and mechanical properties of annealing-induced wrinkles in h-BN flakes are studied with brightfield microscopy, atomic force microscopy, scanning electron microscopy, and Raman spectroscopy.

6.1.1. Topography

Figure 6.2 shows atomic force microscopy images of h-BN flakes with increasing thickness on a Si/SiO_2 substrate, captured before (top row) and after (bottom row) annealing at 1000 °C for 2 hours in high vacuum. The figure illustrates the impact of high temperature annealing on wrinkle generation in h-BN flakes, showing that all flakes exhibit an increase in wrinkle density post-annealing. With wrinkle density defined as the total wrinkle length per unit area. Additionally, high temperature annealing effectively removes residual glue from the stamping process, as most clearly seen in Figure 6.2a, which is important for minimizing background fluorescence.

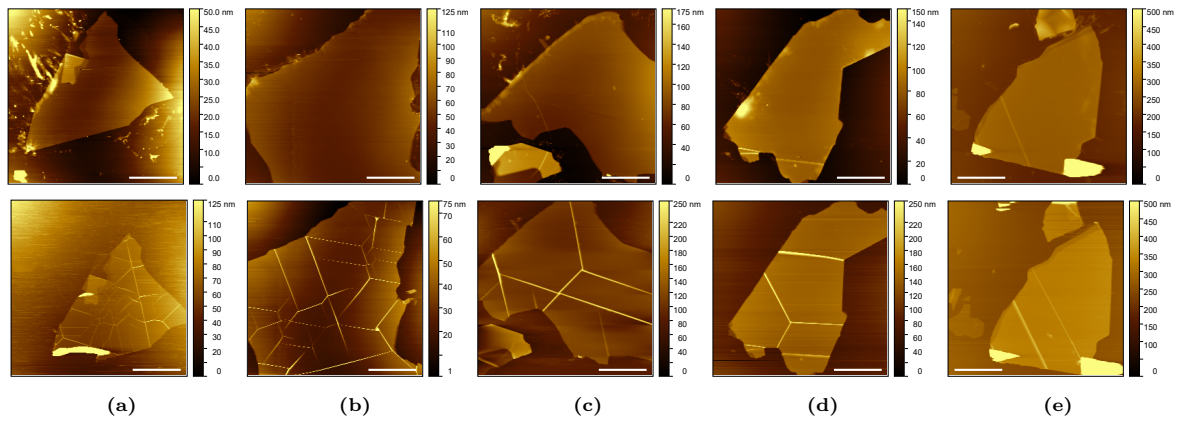

Figure 6.2: Atomic Force Microscopy (AFM) images of hBN flakes of various thicknesses on Si/SiO_2 before and after annealing in high vacuum at 1000°C for 2 hours. The colorbar is scaled differently for all flakes for visibility. The inset scalebar represents 20 µm. **(a)** 13 **(b)** 24 **(c)** 40 **(d)** 70 **(e)** 110 nm.

To further investigate the influence of the flake thickness and thermal expansion coefficient (TEC) mismatch between h-BN and various substrates on wrinkle density and morphology, multiple flakes with thicknesses ranging from 0 to 120nm were annealed on Si/SiO_2, sapphire (Al_2O_3), and quartz (SiO_2) substrates. Figure 6.3a presents the wrinkle density against flake thickness on Si/SiO_2, sapphire, and quartz substrates post-annealing. The wrinkle densities were determined by manually tracing AFM images of annealed flakes in MATLAB. The graph shows a negative correlation between the wrinkle density and flake thickness across all three substrates. This trend can be attributed to the increasing influence of interlayer electrostatic and van der Waals forces, which become more pronounced as the

number of layers increases, leading to greater bending rigidity in the flakes and consequently inhibiting the formation of wrinkles [92][93].

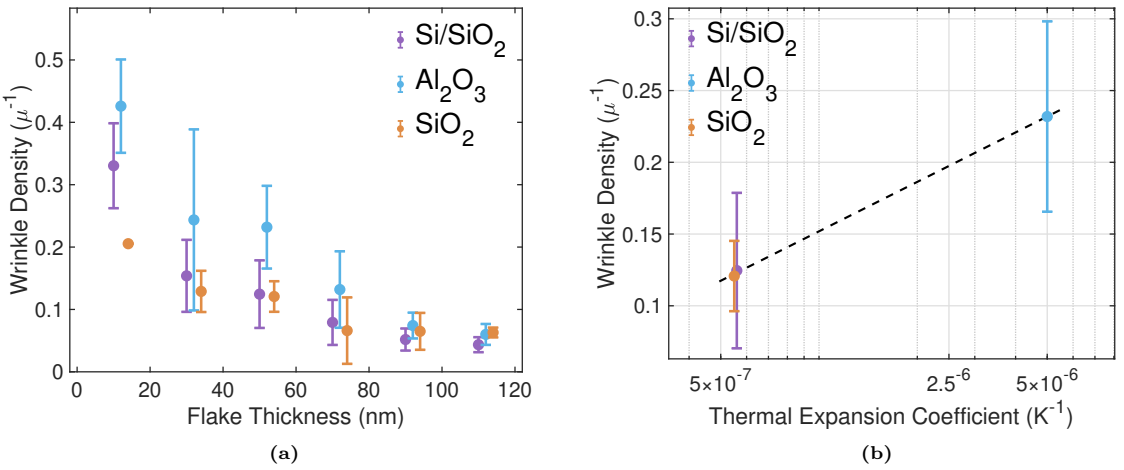

(a) (b)

Figure 6.3: **(a)** Wrinkle density (post-annealing), defined as the total wrinkle length per unit area, against h-BN flake thickness on Si/SiO_2, sapphire (Al_2O_3), and quartz (SiO_2). The flakes are grouped into 20 nm thickness bins, with each bin containing 3 to 5 flakes to compute the mean and standard deviation as error bars. The data points are slightly offset in the x-direction for clarity. **(b)** Mean wrinkle density and standard deviation for 5 annealed flakes with a thickness of 40 to 60 nm against the thermal expansion coefficient of Si/SiO_2(5.6×10^{-7} K^{-1}), quartz (5.5×10^{-7} K^{-1}), and sapphire (5×10^{-6} K^{-1}). The TEC of silicon is also shown at 2.5×10^{-6} K^{-1}.

Figure 6.3b highlights the positive correlation between wrinkle density and the in-plane thermal expansion coefficient (TEC) mismatch between the substrate and h-BN. With h-BN having a TEC of -2.9 $\times$ 10^{-6} K^{-1}, a higher positive TEC for the substrate results in a larger absolute difference in TEC values. The figure presents the mean wrinkle density and standard deviation for annealed flakes within the 40 to 60 nm thickness range, deposited on Si/SiO_2, quartz, and sapphire. Figure 6.3 demonstrates that sapphire consistently generates the highest wrinkle densities across all flake thicknesses. This outcome can be attributed to the significant mismatch in TEC values between sapphire and h-BN, which leads to a higher wrinkle density. In contrast, Si/SiO_2 and quartz substrates produce similar wrinkle densities overall. Notably, the difference in wrinkle densities between substrates becomes less significant as flake thickness increases. This is largely due to the fact that only flakes with at least one wrinkle were included in the analysis, thereby excluding many wrinkle-free flakes on Si/SiO_2 and quartz. Also, flakes below 20 nm were difficult to find on quartz, so only one data point could be obtained.

6.1.2. Morphology

Various wrinkle morphologies were observed across multiple substrates and even within individual flakes. As shown in Figure 6.4, the wrinkles are triangular in shape with relatively sharp bends at the top and bottom.

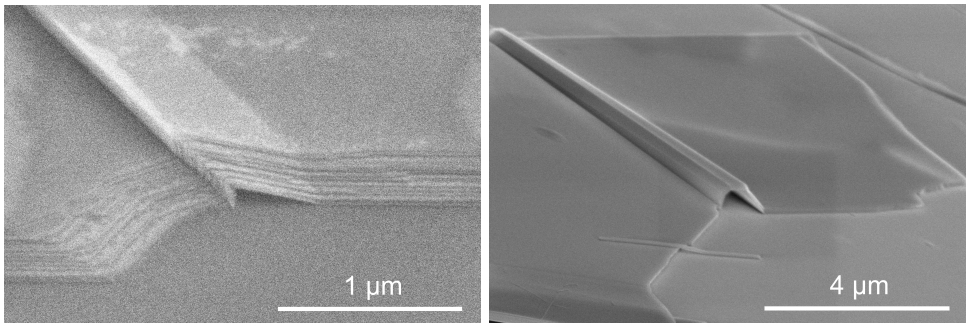

(a) (b)

Figure 6.4: Scanning electron microscopy (SEM) images of wrinkled 2D h-BN flakes on **(a)** Si/SiO_2 **(b)** sapphire.

The complete delamination of the flake from the substrate, along with the fact that nearly all layers conform to the wrinkle profile, clearly indicates strong interlayer bonding from electrostatic and van der Waals forces [94]. In fact, literature reports that the internal shear stress transfer efficiency in h-BN layers is approximately 99%, compared to only 60–80% for graphene [95]. Moreover, the wrinkles have remained stable over time, with no visible slippage. Variations in wrinkle height and width were also observed across the three substrates. Figure 6.5 presents the relationship between wrinkle height and width for annealed flakes within two distinct thickness ranges (20-40 nm and 60-80 nm).

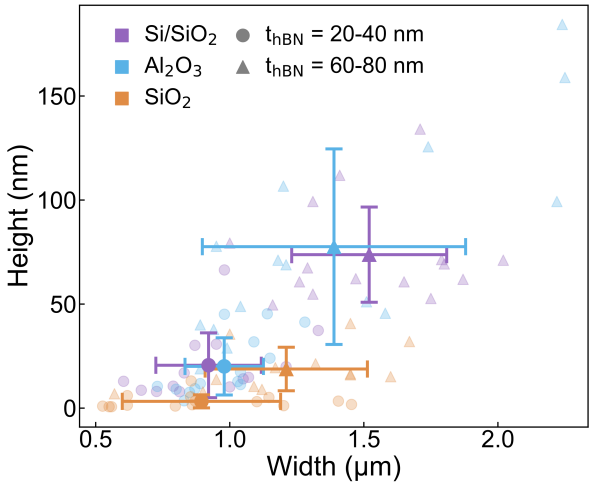

Figure 6.5: Mean and standard deviation of the height and width of wrinkles on Si/SiO_2, Al_2O_3 (sapphire), and SiO_2 (quartz) post-annealing. The flakes are grouped into two 20 nm thickness bins, with each bin containing three flakes per substrate. On each flake, the height and width of five representative wrinkles were measured from AFM data to compute the mean and standard deviation as error bars.

Where Si/SiO_2 and sapphire substrates exhibit similar wrinkle morphologies, with wrinkle height and width significantly increasing with flake thickness, in some cases exceeding 150 nm and 2 µm, respectively. In contrast, quartz produces significantly smaller wrinkles, and flake thickness appears to be less influential on wrinkle height and width compared to the other substrates. The reason for this discrepancy between Si/SiO_2 and quartz is unclear; it may be related to the 525 µm silicon, which has a TEC of 2.5×10^{-6}, underneath the SiO_2 layer and the relative thinness of the 285 nm SiO_2 layer. Additionally, h-BN may bond differently to lab grown SiO_2 compared to fused quartz.

6.1.3. Orientation

The wrinkles in annealed h-BN appear to form distinct patterns. Wrinkles predominantly form three-fold junctions, with occasional four-fold or even five-fold junctions observed. Upon closer inspection, it was found that the wrinkles, in some cases, connected through a small rotated triangle as shown in Figure 6.6a, a feature also reported by Oliveira et al. [78]. In most cases, the connections between wrinkles were irregular as seen in Figure 6.6b.

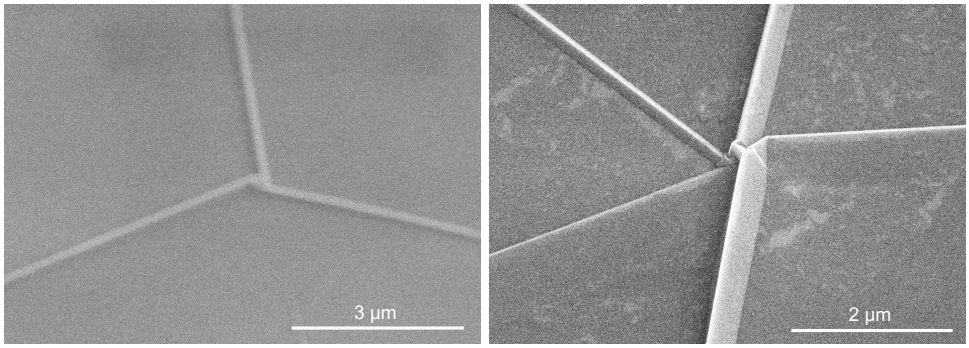

(a) **(b)**

Figure 6.6: SEM images of wrinkle junctions on Si/SiO_2. **(a)** A three-fold wrinkle junction connected through a small rotated triangle **(b)** A five-fold junction with an irregular connection pattern.

To further investigate these patterns, the angular separation between the wrinkles was analysed. Figure 6.7 shows a histogram of wrinkle angles relative to the horizontal direction θ. First, angles were determined by manually tracing wrinkles in AFM data collected from three annealed h-BN flakes of similar thickness (25–35 nm). Equation 6.1 was used, where α is the measured wrinkle angle from which 180° is subtracted to account for symmetry.

$$\theta = |\alpha - 180°| \tag{6.1}$$

Three prominent peaks were observed and fitted with Gaussian distributions, with their mean values approximately 60° apart. Additionally, two smaller groups of gray bins appear, roughly 30° offset from the prominent peaks. Given that h-BN has two crystallographic directions, armchair and zigzag, separated by 30°, it can be inferred that wrinkles preferentially form along one of these directions, while occasionally aligning with the other direction.

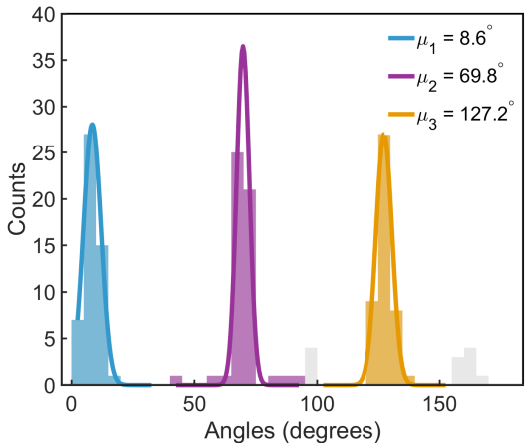

Figure 6.7: Histogram showing the angular distribution of wrinkles in annealed h-BN flakes. The angles α were calculated using Equation 6.1 w.r.t. the horizontal direction. Three prominent peaks appear, which have been fitted with Gaussian distributions. The mean values of the distributions are $\mu_1 = 8.6°$, $\mu_2 = 69.8°$, and $\mu_3 = 127.2°$.

To provide further evidence for the preferential alignment of wrinkles with the crystallographic directions of h-BN, and in an attempt to identify which direction is favoured, Raman spectroscopy measurements were conducted using a polarized laser setup [96][97]. Figure 6.8a shows an h-BN flake on Si/SiO_2 with a sharp 90° corner, which strongly suggests that the edges align with different crystallographic directions, zigzag and armchair, as flakes commonly fracture along these orientations. By aligning both edges separately with the polarization direction of the laser, it was hypothesized that the edges would show different Raman signatures depending on the alignment, as is the case for graphene [97][98] and other 2D materials [96]. Then, we could subsequently align the wrinkles with the polarization direction of the

laser and compare their Raman signatures. Figures 6.8b and 6.8c show the E_{2g} Raman peak intensity maps of the flake corner for 0° and after a 90° clockwise rotation. Both edges showed maximum peak intensity when aligned with the laser polarization, making them indistinguishable through this method. This result contrasts with graphene, where the armchair edge exhibits maximum intensity when aligned with the laser and minimum intensity when rotated by 90°, while the opposite behaviour is observed for the zigzag direction. Therefore, this method was deemed unsuitable for determining the preferred crystallographic direction for wrinkle formation in h-BN flakes at this stage.

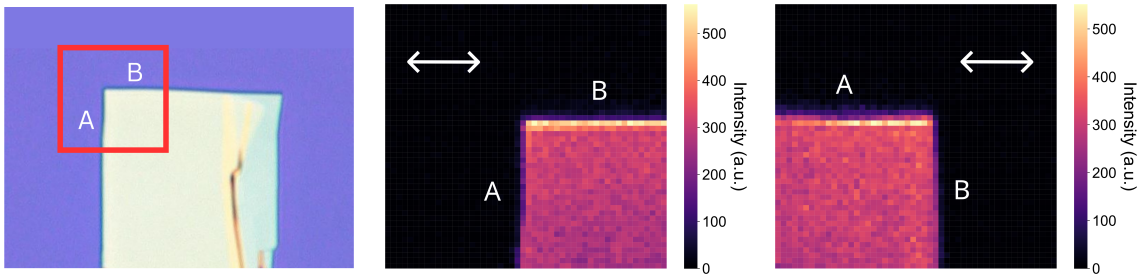

(a) **(b)** **(c)**

Figure 6.8: Raman intensity map of the E_{2g} vibrational mode on an h-BN flake with a 90° corner. **(a)** Optical image of the h-BN flake with the measured area indicated by the red square. The laser polarization direction is indicated by the arrow. In **(c)** the flake is rotated 90° clockwise relative to **(b)**.

6.1.4. Strain

Here, we utilize Raman spectroscopy to study the strain distribution in wrinkles. First, the in-plane E_{2g} Raman peak of bulk h-BN crystal was measured as a reference for unstrained h-BN. By analyzing the same Raman peak in wrinkled h-BN flakes and comparing its width, height, and position, the presence and magnitude of strain within the wrinkled flakes can be assessed. Figure 6.9 shows the Lorentzian fitted E_{2g} Raman peak measured at ten different positions across two h-BN crystals. A Lorentzian function was chosen because it is widely used in the literature to fit the E_{2g} peak [56][99]. The mean value of the peak position was found to be at 1365.5 ± 0.3 cm^{-1} which is slightly red-shifted compared to values found in literature for bulk h-BN (1366.2 ± 0.2 cm^{-1} [56]). This could have to do with the calibration of the Raman spectrometer or pre-existing strain in our bulk crystals. The full width at half maximum of the peak (FWHM) of 8.2 ± 0.1 cm^{-1} matches with values found in literature for bulk h-BN [53][100].

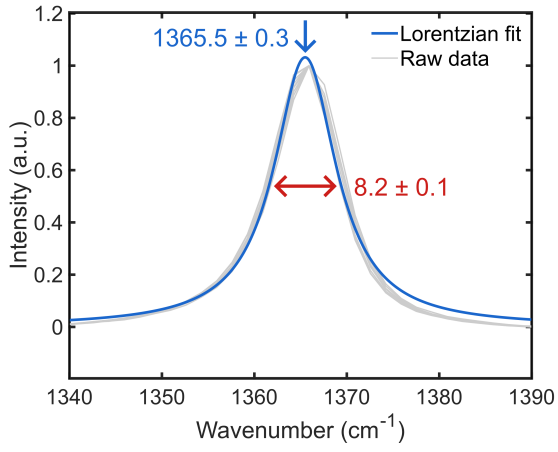

Figure 6.9: Normalized intensity of the E_{2g} Raman peak of bulk h-BN crystal. Measurements were taken across ten points using a 532 nm laser with an exposure time of 10 s, laser power of 5%, and 20 accumulations. The raw data (in gray) was fitted by a Lorentzian distribution (in blue) which has a mean value of 1365.5 ± 0.3 cm^{-1} and a FWHM value of 8.2 ± 0.1 cm^{-1}.

Figure 6.10 presents a 3D view of an AFM measurement of a thermally induced three fold wrinkle

junction on an h-BN flake deposited on a Si/SiO_2 substrate annealed in high vacuum, which was analysed to investigate its strain distribution.

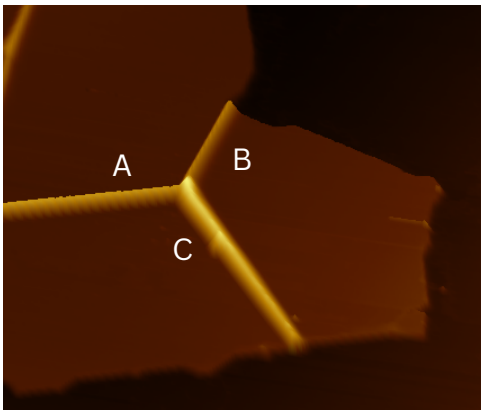

Figure 6.10: An AFM image of the wrinkle junction selected for strain distribution analysis is shown, with the three wrinkles labelled for easier identification.

Figure 6.11a presents the variation in peak position of the E_{2g} phonon mode at the wrinkle junction in Figure 6.10. This map was generated by fitting the E_{2g} Raman peak with a Lorentzian distribution and plotting the mean value at each point. Similarly, the variation in the FWHM of the peak is plotted in Figure 6.11b.

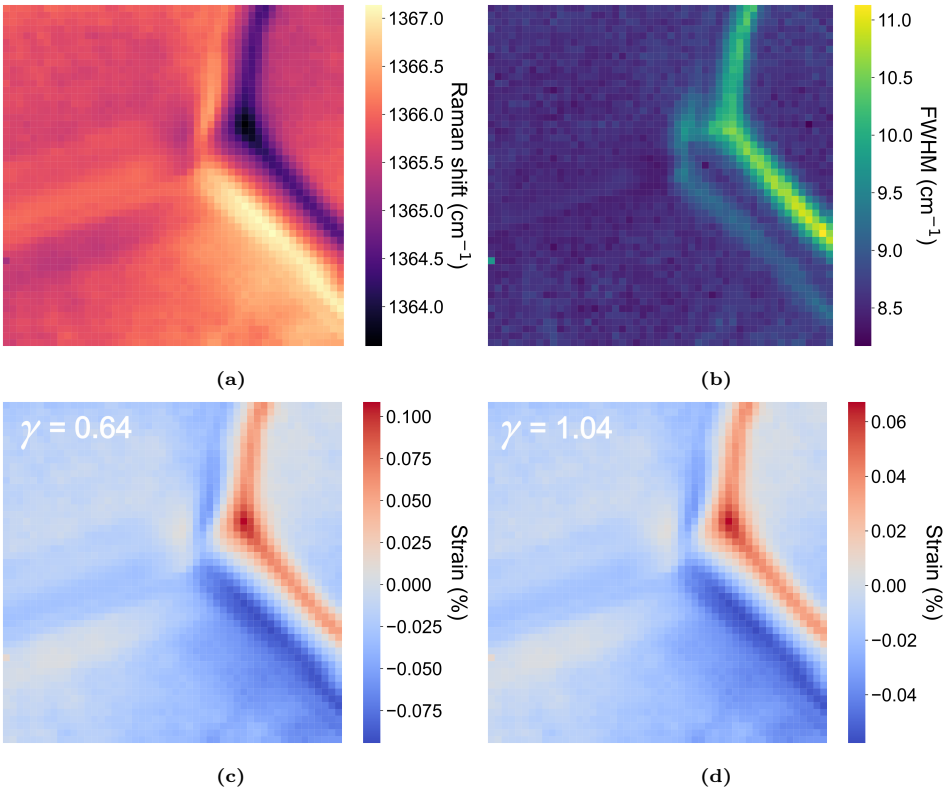

Figure 6.11: Heatmap illustrating the Raman signature of an h-BN wrinkle junction on Si/SiO_2 post-annealing. The mapped area measures 15 µm × 15 µm with a spatial resolution of 0.3 nm. Raman mapping was conducted using a 488 nm laser, with an exposure time of 8 seconds and three accumulations per measurement. The h-BN Raman peak was fitted using a Lorentzian function within the range of 1340–1390 cm^{-1}, and the resulting peak positions are displayed in the heatmap. **(a)** Variation in the E_{2g} peak position. **(b)** Full width at half maximum. **(c,d)** Strain distribution for Grüneisen parameter $\gamma = 0.64$ and 1.04.

The strain distributions shown in Figures 6.11c and 6.11d, were calculated using Equation 6.2. Since

no splitting of the E_{2g} peak was observed, it was assumed that the strain in the h-BN flakes was purely biaxial [56], with $\varepsilon_{tt} = \varepsilon_{ll}$, allowing Equation 2.2 to be simplified to Equation 6.2 to calculate residual strain ε_r. Because a wide range of Grüneisen parameter values (γ) for h-BN have been reported in literature, both values of 0.64 [101] and 1.04 [99] were taken for this calculation. The value for unstrained bulk h-BN ω^0 was previously determined to be 1365.5 cm^{-1}.

$$\varepsilon_{ll} = \varepsilon_{tt} = \varepsilon_r = \frac{-\Delta\omega}{2\gamma\omega^0} \tag{6.2}$$

In Figure 6.11, both tensile (red) and compressive (blue) strain are visible. A positive $\Delta\omega$ (blue shift in Raman wavenumber) indicates compressive strain, while a negative $\Delta\omega$ corresponds to tensile strain. As discussed in Section 6.1.4, the compressive strain in h-BN induced by high temperature annealing ε_{th} can be estimated using Equation 6.3.

$$\Delta\varepsilon_{th} = \int_{T_1}^{T_2} (\alpha_s - \alpha_f)\delta T \tag{6.3}$$

For h-BN on a Si/SiO_2 substrate, heated from 20°C to 1000°C, the maximum thermal strain ε_{th} reaches -0.31%. Note that the influence of the underlying Si is neglected in this calculation. In flat regions, only a residual compressive strain of approximately -0.03% is left, demonstrating that wrinkling effectively relieves the thermally induced compressive strain. The highest residual strain values are concentrated at wrinkles B and C, but depending on the Grüneisen parameter used in the calculation, the maximum residual strains at the wrinkles vary. Using $\gamma = 0.64$, the maximum tensile and compressive strains are 0.109% and -0.094%, respectively; for $\gamma = 1.04$, they are 0.067% and -0.058%, respectively. Closer examination with SEM reveals that these wrinkles are particularly wide, 2.7 and 4.4 µm for wrinkle B and C, respectively. As shown in Figure 6.12, they feature a large, slightly curved suspended area, which could account for the observed tensile strain.

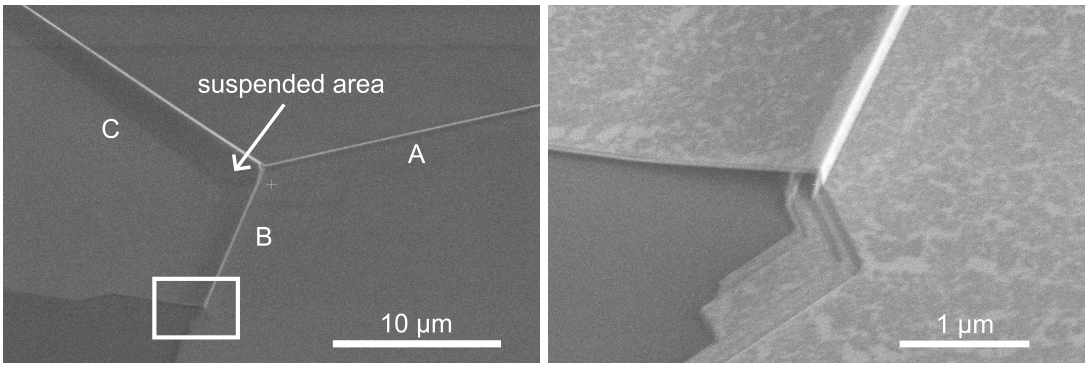

(a) **(b)**

Figure 6.12: SEM images of the wrinkle junction. **(a)** The darker area indicated by the arrow is the suspended part between wrinkles B and C. **(b)** Zoomed in area of wrinkle B, indicated by the white square in **(a)**.

Figure 6.11b illustrates the variation in the FWHM distribution along the wrinkles, where an increase in FWHM may suggest local strain or reduced crystallinity in the flake [102][103]. Notably, the FWHM in the area between wrinkles B and C is up-shifted by approximately 3 cm^{-1} relative to the unstrained bulk value of 8.2 ± 0.1 cm^{-1}, while the FWHM for wrinkle A remains nearly unchanged.

These results reveal that wrinkling can create local strain regions, potentially serving as sites for quantum emitter localization. Moreover, variations in Raman signatures among wrinkles indicate differences in strain distribution, offering a degree of spatial and spectral control.

6.2. Characterization of Quantum Emitters

The photophysical properties of optically active defects in the wrinkled h-BN flakes are studied with fluorescence microscopy and photoluminescence spectroscopy. It was decided to continue with the Si/SiO_2 substrate as sapphire's fluorescence causes much background signal and the wrinkles on quartz were relatively small.

6.2.1. Optical Properties

To localize the quantum emitters at the wrinkle junction analyzed in Section 6.1.4, fluorescence microscopy measurements were taken in three wavelengths. Figure 6.13 shows the averaged pixel intensity images, in which features that appear brighter exhibit more fluorescence. The image stack was recorded with an exposure time of 100 ms per frame, for 40 seconds. For all three wavelengths, the bright, three-fold wrinkle junction is clearly visible, demonstrating that the wrinkles fluoresce more strongly than the flat h-BN surface—with green and blue exhibiting the most intense emissions. Additionally, wrinkles B and C display greater fluorescence activity, with the brightest emitters concentrated near their edges where the highest tensile/compressive strain was measured. Interestingly, blue emitters tend to cluster close to the center of the junction, while red and green emitters are more prevalent away from it.

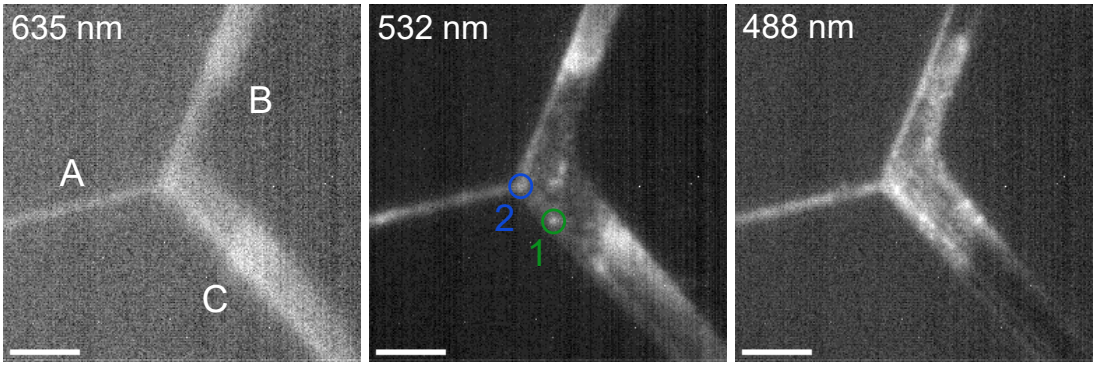

(a) **(b)** **(c)**

Figure 6.13: Epi-fluorescence microscopy images of wrinkle junction A for: **(a)** Red laser (635 nm) **(b)** Green laser (532 nm) **(c)** Blue laser (488 nm). The inset scale bar represents 50 µm.

Overall, the emitters exhibited relatively high photostability. Two exceptional intensity profiles—one showing bleaching (1) and the other blinking (2)—from Figure 6.14a are presented in Figure 6.14. Even in these cases, both bleaching and blinking occur gradually rather than abruptly.

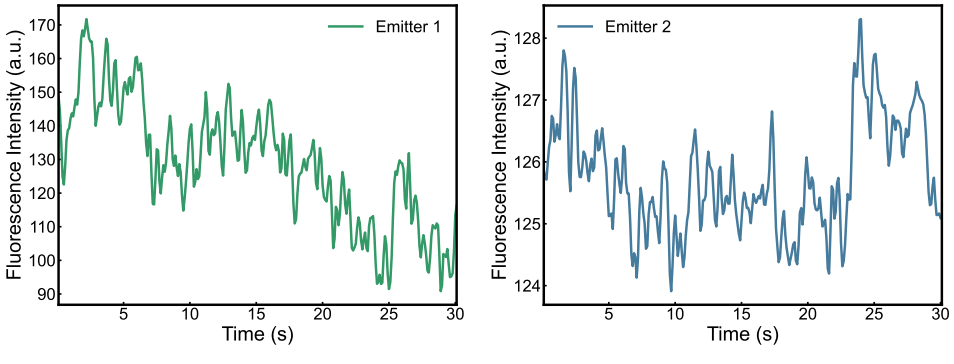

(a) **(b)**

Figure 6.14: Fluorescence intensity of two fluorescent features marked by circles in Figure 6.13b over a 30 second time period. **(a)** Fluorescence intensity gradually decreasing over time (bleaching). **(b)** Fluorescence intensity decreasing and increasing over time (blinking).

6.2.2. Spectral Properties

Photoluminescence spectra were recorded to study the emission energies of emitters localized at the wrinkles in Figure 6.13 more in depth. Figure 6.15 displays PL intensity maps at 580, 620, and 660 nm. Due to long acquisition times, the mapping area was limited, and a system offset caused wrinkle B to largely fall outside the mapped region. Although strong emission was observed in blue in Figure 6.13, which would have been interesting to map, the 488 nm laser was not selected because it is only compatible with the 3000/mm grating, which would significantly restrict the spectral range. In stead, a 514 nm laser with an 1800/mm grating was used for the PL measurement over a spectral range of 550-670 nm.

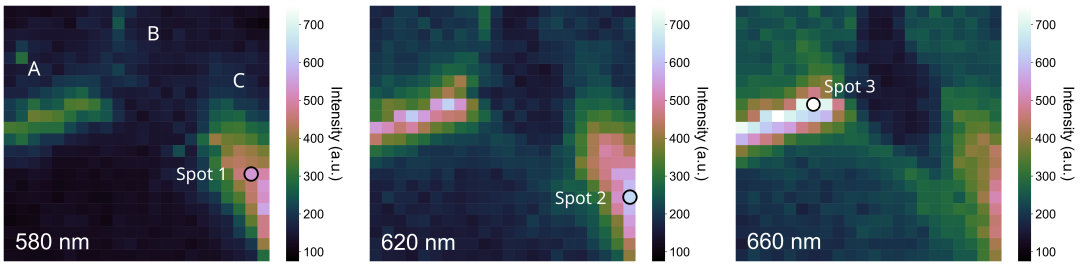

(a) **(b)** **(c)**

Figure 6.15: Photoluminescence intensity maps of the h-BN wrinkle junction on a Si/SiO_2 substrate. Three wavelengths are plotted: **(a)** 580 nm **(b)** 620 nm **(a)** 660 nm. The spectra were taken using a 514 nm laser with an exposure time of 10 seconds and 5% power. The mapped area measures 9 µm × 9 µm with a spatial resolution of 0.3 nm. As seen in previous figures, the wrinkles are labelled A, B, and C.

The maps show that emitters are localized at the wrinkles, with different emission wavelengths corresponding to distinct regions. This observation is consistent with the fluorescence microscopy data; however, the photoluminescence (PL) data reveals a slightly different emission distribution. A darker region remains around the junction center, yet red emission is notably enhanced compared to green, particularly along wrinkle A. Representative PL spectra taken from the three locations marked in Figure 6.15 are shown in Figure 6.16. The E_{2g} phonon mode is distinctly observed at 553 nm. The figures exhibit broad spectral peaks without sharp zero phonon lines (ZPL), except for the peak near 560 nm in Figure 6.16c showing up next to the E_{2g} phonon mode. This makes it difficult to properly characterize the emitters and associate the observed emissions with specific defect types. Small local strain variations may have shifted the emission energies of the emitters over a broader range [74], or contamination on the wrinkles might be responsible, given that this map was taken a few days after the fluorescence measurements.

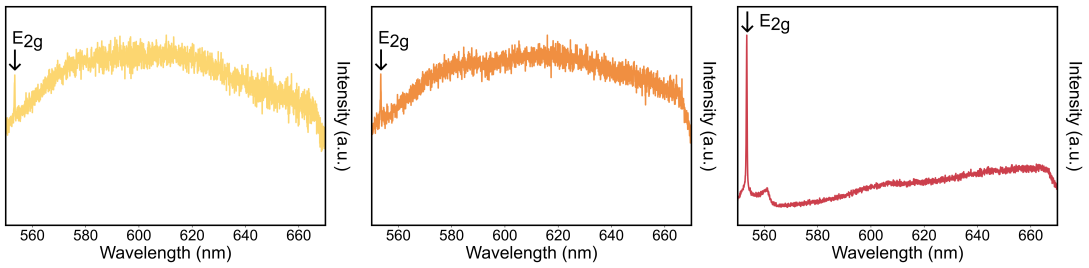

(a) **(b)** **(c)**

Figure 6.16: Three respresentative PL spectra taken at three different spots in the PL maps: **(a)** spot 1 **(b)** spot 2 **(c)** Spot 3. The E_{2g} Raman peak at 553 nm is indicated by an arrow.

To investigate whether this observation could related to the high vacuum annealing environment, another flake annealed in 200 sccm argon at 1000 °C for 2 hours was analysed. Figure 6.17 presents the averaged pixel intensity images of the wrinkled flake after annealing. Similar to the flake annealed in high vacuum, fluorescence activity concentrates along the wrinkles for all three wavelengths. In certain areas, emitters seem to cluster at specific points along the wrinkles. Following this, a PL line map was acquired along the central wrinkle, as indicated by arrows in Figure 6.17b.

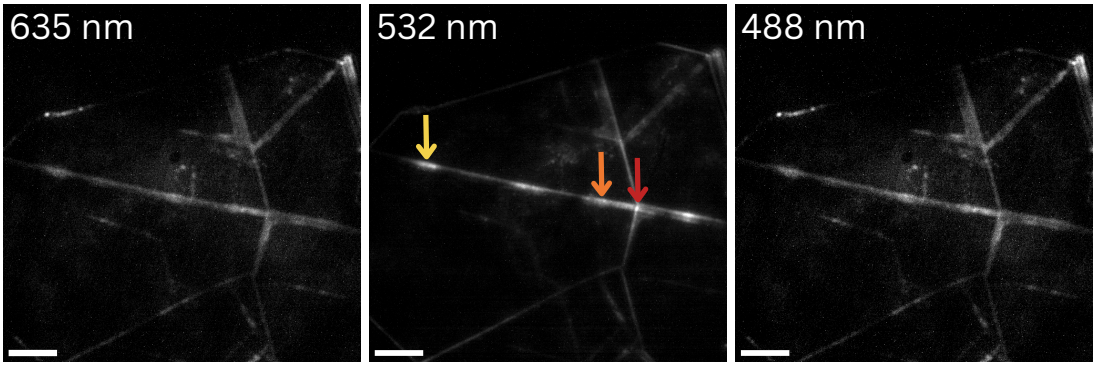

(a) (b) (c)

Figure 6.17: Epi-fluorescence microscopy images of an h-BN flake annealed in 200 sccm argon at 1000 °C for 2 hours. **(a)** Red laser (635 nm) **(b)** Green laser (532 nm) **(c)** Blue laser (488 nm). The inset scale bar represents 10 µm.

Figure 6.18 presents three PL spectra taken from the locations marked by arrows in Figure 6.17b, with each spectrum color-matched to its corresponding arrow. The argon annealed emitters show distinct zero-phonon lines (ZPLs), contrasting with the PL spectra seen from high vacuum annealing. The E_{2g} Raman peak shows again around 553 nm. These relatively sharp ZPLs around 570, 610, and 620 nm can possibly be attributed to vacancy type defects and carbon-related defects. This comparison suggests that the annealing environment may influence the ZPL characteristics of emitters in wrinkles. However, since only two flakes were examined, further research with additional samples is necessary to draw a more definitive conclusion.

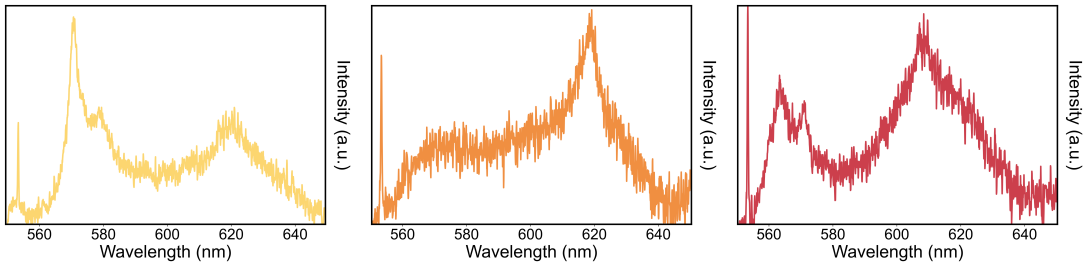

(a) (b) (c)

Figure 6.18: Three PL spectra taken at three different spots in a PL line map of the argon annealed flake: **(a)** yellow arrow **(b)** orange arrow **(c)** red arrow. The E_{2g} Raman peak shows up again at 553 nm.

6.3. Optofluidic Experiment

Since biomolecules are typically in solution, it is of interest to investigate how wrinkles and emitters behave in such environments. In a previous study, Ronceray et al. [104] found that quantum emitters in pristine h-BN flakes could be optically activated by organic solvents like ethanol through chemisorption of the solvent's molecules onto the native defects, whereas pure water did not produce the same effect. Inspired by these findings, annealed flakes were characterized by measuring their fluorescence first in air and then exposed to water or ethanol. Figure 6.19 shows a schematic of the measurement setup that was used in these experiments.

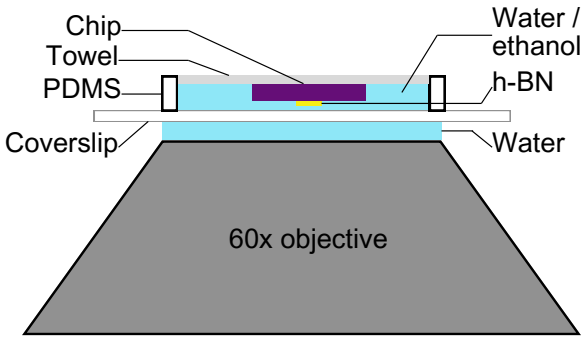

Figure 6.19: Schematic depicting the optical microscope setup used for experiments in water and ethanol. The h-BN sample facing the objective lens, through which the excitation light is transmitted and the reflected light is collected. A small piece of cleanroom towel is soaked placed on top to prevent the chip from floating.

6.3.1. Experiment in Water

Figure 6.20a displays microscopy data of an h-BN flake in both air and water, epi-illuminated by white light with an exposure time of 10 µs. The wrinkles remained intact, showing no collapse or significant structural deformation. In stead, they appeared more pronounced and broadened in water, indicating that water might be present inside the wrinkles. Dark spots across the flake also suggest that water may have seeped between the flake and the substrate. Figures 6.20b, 6.20c, and 6.20d present the averaged fluorescence intensity over a 20 second image stack, taken with an exposure time of 100 ms (totalling 200 frames). For all three wavelengths, fluorescence intensity is highest along the wrinkles compared to the flat h-BN. A small concentration of emitters is also observed along the flake edges. Upon water exposure, the fluorescence intensity on the wrinkles increases, and new activity emerges in some flat regions. This finding is particularly interesting, as Ronceray et al. did not observe any fluorescence activity after water exposure.

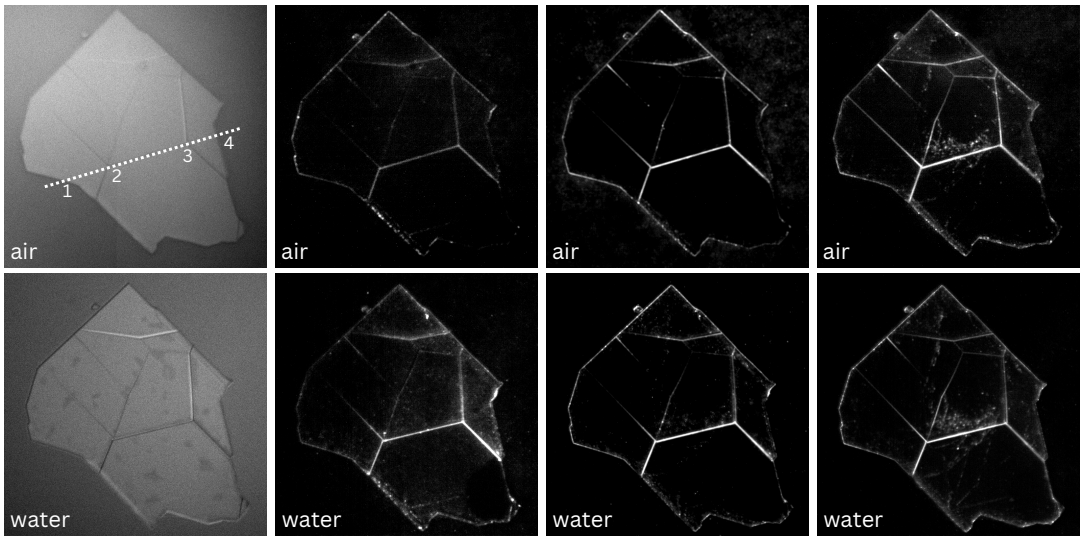

Figure 6.20: Epi-fluorescence microscopy images in air and water of an h-BN flake that was annealed in high vacuum. Images are taken in: **(a)** White **(b)** Red laser (635 nm) **(c)** Green laser (532 nm) **(d)** Blue laser (488 nm).

Figure 6.21 presents quantitative data on the flake's increased fluorescence in water. The plot along the dotted line in Figure 6.20a for all three wavelengths shows a clear intensity rise and new peaks, indicating additional emitters are activated. Note that along this line, the flat region shows minimal change, suggesting water primarily affects emitters on the wrinkles.

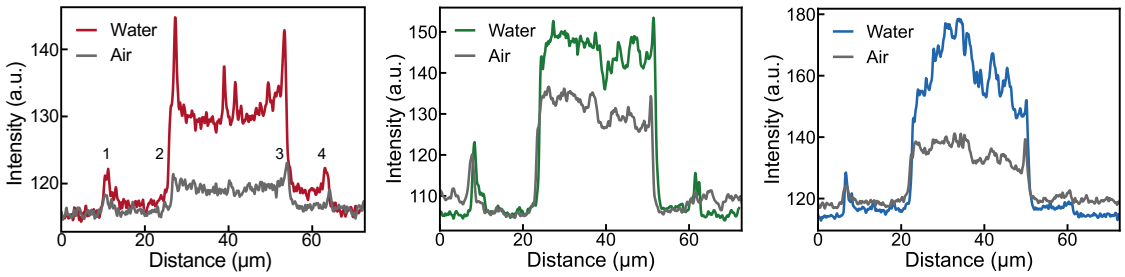

Figure 6.21: Fluorescence pixel intensity in air and water across the wrinkle marked by the line in Figure 6.20a for the three wavelengths **(a)** Red laser (635 nm)**(b)** Green **(c)** Blue laser (488 nm).

6.3.2. Experiment in Ethanol

The experiment was repeated on a different flake with ethanol in stead of water. Figure 6.22 displays the flake under white light alongside the averaged fluorescence intensity images. The results resemble those observed with water, showing increased intensity of active emitters on the wrinkles and the activation of new emitters upon ethanol exposure.

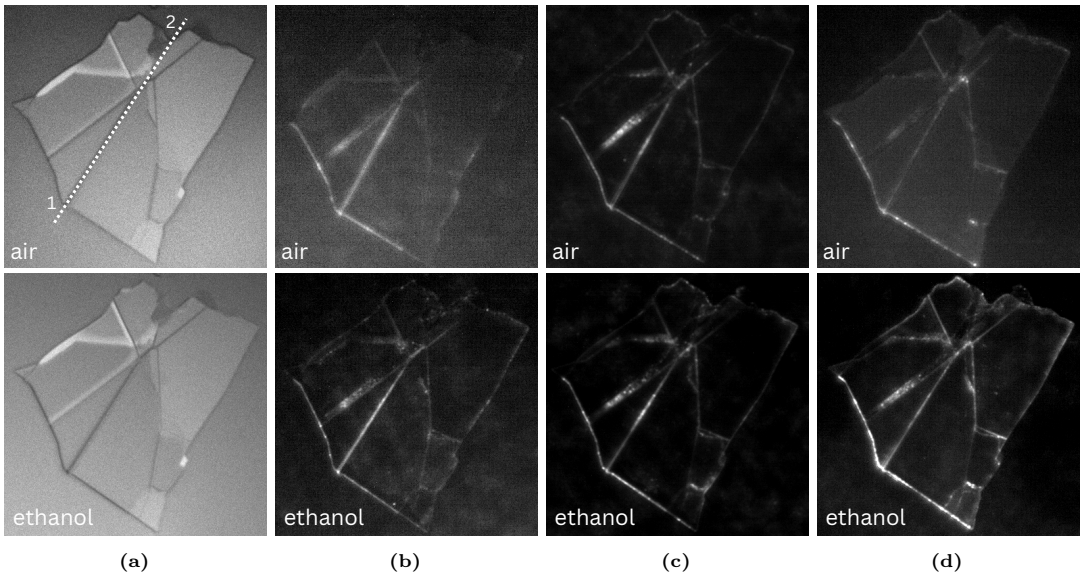

Figure 6.22: Epi-fluorescence microscopy images in air and ethanol of an h-BN flake that was annealed in high vacuum. Images are taken in: **(a)** White **(b)** Red laser (635 nm) **(c)** Green laser (532 nm) **(d)** Blue laser (488 nm).

Figure 6.23 provides quantitative data on the flake's fluorescence enhancement in ethanol. In this case, the plot along the dotted line in Figure 6.22a indicates a less pronounced intensity increase for all three wavelengths. While some new emitters are activated, others appear to be quenched. Unlike the scenario in water, the flat region exhibits almost no activation of new emitters.

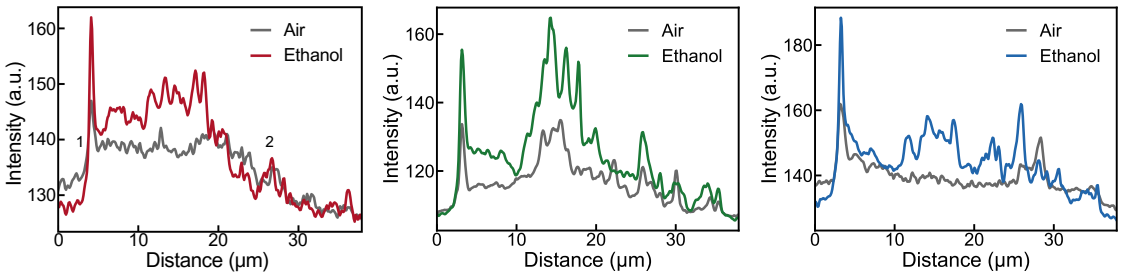

(a) (b) (c)

Figure 6.23: Fluorescence pixel intensity in air and ethanol across the wrinkle marked by the line in Figure 6.22a for the three wavelengths **(a)** Red laser (635 nm)**(b)** Green **(c)** Blue laser (488 nm).

Figure 6.24 displays the flake before and after ethanol exposure. In Figure 6.24b, the flake was initially removed from the PDMS window and briefly dried with an air gun. Despite this, the wrinkles remain widened, suggesting the presence of residual ethanol. Five days later, Figure 6.24c was taken, showing that nearly all ethanol has evaporated from the flake's surface. While the wrinkles appear thinner, they remain wider than before ethanol exposure, indicating either permanent deformation or the retention of residual liquid due to intermolecular forces counteracting complete evaporation.

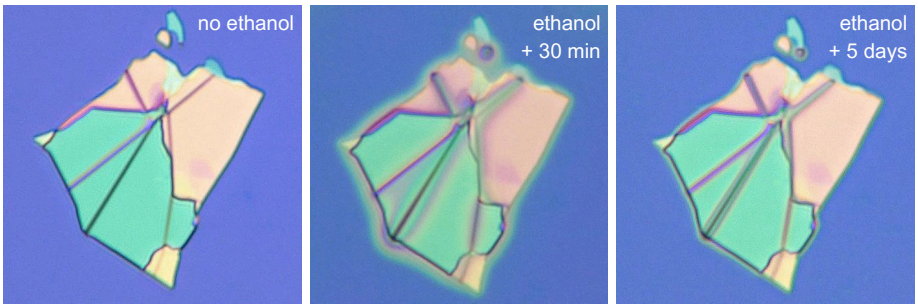

(a) (b) (c)

Figure 6.24: Bright-field microscopy images of the wrinkled h-BN flake exposed to ethanol. **(a)** before **(b)** after 30 minutes **(c)** after 5 days.

7
Conclusions and Outlook

This chapter concludes the study by summarizing the key research findings in relation to the research questions outlined in Chapter 4.

> *What are the characteristic structural properties of wrinkles in 2D hexagonal boron nitride flakes, and how do these features relate to the photophysical properties of quantum emitters in the context of optofluidic applications?*

It also discusses its limitations and suggests directions for future research

7.1. Conclusions

The three sub-questions, formulated in Section 4 to answer the main research question, are answered here below.

What are the detailed structural properties of wrinkles in 2D h-BN flakes, and how are these features influenced by the substrate material?

> Thermal annealing at 1000 °C for 2 hours proved to be an effective method for consistently generating wrinkles in 2D h-BN. The results showed that across all substrates, the wrinkle density was found to be negatively correlated with flake thickness. Among the three tested substrates, flakes annealed on sapphire (Al_2O_3) exhibited the highest wrinkle densities compared to Si/SiO_2 and quartz (SiO_2) substrates. While different wrinkle morphologies were observed, the wrinkles were generally triangular in shape, with excellent stress transfer indicated by the collective wrinkling of most layers. Wrinkle height and width showed a positive correlation with flake thickness, and aspect ratios were similar for sapphire and Si/SiO_2 substrates with wrinkles over 150 nm high and more than 2 µm wide, whereas quartz produced significantly smaller wrinkles. Additionally, the wrinkles seemed to preferentially align with one of the crystallographic orientations of h-BN, following either the armchair or zigzag direction, as indicated by their angular separation (in multiples) of 60°. An attempt to use polarized Raman spectroscopy to determine the preferred edge structure was unsuccessful due to the similar Raman signatures of both edge types.

What are the photophysical properties of wrinkles in 2D h-BN flakes, and how do these relate to the identified structural properties of the wrinkles?

> Fluorescence microscopy data revealed that quantum emitters predominantly localize on wrinkles compared to the flat h-BN surface. This was consistently observed across different emission wavelengths, including red (635 nm), green (532 nm), and blue (488 nm), suggesting a correlation between the structural features of wrinkles and the photophysical behaviour of the emitters. Further photoluminescence mapping supported these observations, showing clear emitter localization along the wrinkles. Emitters annealed in high vacuum exhibited broad emission spectra without distinct zero-phonon lines (ZPLs), whereas emitters annealed in argon displayed sharp ZPLs within the 570–670 nm range. The underlying cause of this discrepancy remains uncertain, though the broader spectral peaks found in the high vacuum annealed sample may be attributed to local strain variations or contamination. Finally, the

emitters exhibited high photostability, with minimal blinking or bleaching observed over a 40-second timeframe.

How does the presence of liquid affect the structural properties of wrinkles in 2D h-BN flakes and the corresponding photophysical properties of quantum emitters?

Preliminary experiments demonstrated that exposure to water and ethanol did not structurally damage or collapse the wrinkles. Instead, the wrinkles widened, suggesting the presence of liquid within them. After leaving the sample in air for five days, most of the ethanol had evaporated from the flake surface; however, the wrinkles remained noticeably wider than before ethanol exposure, implying that intermolecular forces may resist complete evaporation of the trapped liquid. Interestingly, the fluorescence intensity of the emitters on the wrinkles increased significantly following exposure to water and ethanol. This finding is unexpected, as Ronceray et al. [104] reported emitter activation in ethanol but not in water. This result suggests that the mechanism enhancing emitter fluorescence may differ from the mechanism responsible for activation.

7.2. Outlook

This outlook reflects on the limitations and challenges encountered during the project while also looking ahead to potential research directions for the future.

7.2.1. Limitations and challenges

1. **Methodology** - Background fluorescence from substrate contamination was a recurring issue in this project. Various potential sources, such as outgassing from the annealing boat and tube, were identified and ruled out one by one. Towards the end of the project, samples were briefly pre-annealed on a hotplate (approximately 10 minutes at 450 °C) to remove most of the glue residue—a by-product of the tape exfoliation process—from the substrate. Subsequent high-temperature annealing significantly reduced the background fluorescence. This suggests that although the glue evaporates in the furnace, the absence of flow allows it to remain in the quartz tube and redeposit on the substrate. Thus, pre-annealing may help prevent contamination during high-temperature vacuum annealing. Additionally, annealing in a flowing gaseous environment such as argon might further reduce contamination, though more experiments are needed to confirm this observation. Supporting figures are provided in Appendix A.
2. **Characterization of Wrinkles** - The statistical significance of the data presented in Section 6.1 is questionable by the small sample size, and additional samples are needed to improve confidence. For example, only one data point was collected for quartz in the thinnest thickness bin. Also, wrinkles for Figure 6.5 were subjectively chosen. Furthermore, several flakes—especially those with higher thicknesses—did not exhibit wrinkles post-annealing and were consequently excluded from the dataset. Investigating why some flakes remain wrinkle-free, while similar ones develop wrinkles, would improve the reliability and robustness of the high temperature annealing method. Lastly, our attempt to resolve the armchair and zigzag crystallographic edges of h-BN by analyzing the intensity of the E_2 Raman peak using polarized Raman spectroscopy remains inconclusive. Alternative methods that have proven effective in literature include second-harmonic generation (SHG) [105][78], decoration with self-assembled octadecylphosphonic acid (OPA) molecules [78], and transmission electron microscopy (TEM) [79], all of which can help determine the exact orientation of the wrinkles relative to the crystallographic edge structures of h-BN.
3. **Characterization of Quantum Emitters** - This study's quantitative analysis of quantum emitters on h-BN wrinkles remains limited. To draw more robust conclusions, additional samples should be annealed in both high vacuum and argon environments and then analyzed. As mentioned earlier, contamination was a recurring issue, but pre-annealing may offer a solution for acquiring a more comprehensive dataset.
4. **Optofluidic Experiment** - The PDMS window used was not ideal, as it was difficult to ensure the flakes were fully immersed in the liquid. Additionally, sample tilting due to floating in combination with the microscope's limited working distance (300 µm) made focusing challenging. A

microfluidic flow cell would offer more control for liquid experiments, reduce evaporation, and actively drive liquid to enter the wrinkles. Furthermore, in this study, wrinkled flakes were exposed to water and ethanol. However, since biomolecules are typically contained in buffer solutions with different chemical properties to water and ethanol, these differences could influence the behaviour of both the wrinkles and the quantum emitters. Investigating these effects is crucial for adapting this technology for biomolecule sensing applications. Lastly, this experiment does not provide solid proof that the wrinkles were actually filled with liquid. To further verify this, fluorescent microbeads could be used to assess whether they enter the wrinkles, or dielectric constant measurements could be conducted. Notably, in confined spaces of 10–1000 nm, the dielectric constant of water is significantly lower than its bulk value [106].

7.2.2. Future research directions

1. **Controlled Wrinkle Networks** - One group reported stimulated wrinkle formation in defective areas of h-BN flakes such as cracks, where there is a local stress concentration [93]. Although, in our study, wrinkles were observed to form in well-defined patterns , such as three-fold Y-junctions, these patterns appear ubiquitously across the flake. Therefore, it would be interesting to design and fabricate defect patterns —aligned with the crystallographic directions of h-BN —to stimulate controlled wrinkle growth and the creation of pre-defined wrinkle networks.
2. **Rapid Thermal Annealing** - It is now thought that wrinkles in 2D h-BN form under thermally induced compressive strain during the cooling down phase of the annealing cycle. In this study, the heater was simply turned off while still being over the region of the annealing tube where the sample sits. It would be interesting to investigate different heating/cooling rates using e.g. a rapid thermal annealing (RTA) furnace, to see if there is any effect on the structural properties of the wrinkles and the photophysical properties of the quantum emitters. Or by simply moving the heater away upon cooling down. Other groups have also explored alternative approaches, such as dipping graphene flakes on PDMS into liquid nitrogen [107].
3. **In-situ Measurements** - In situ characterization of wrinkles during the annealing cycle could offer additional insights into the mechanism of wrinkle formation and their structural properties, including their initiation sites and the evolution of strain distribution. A Linkam stage like the TS1200, which is compatible with the Renishaw inVia microscope, could be employed for this purpose.
4. **Buckling-induced Delamination** - To potentially achieve greater control over wrinkle morphology and to explore the possibility of dynamically tuning or even reversing wrinkle formation, employing buckling-induced delamination could be an interesting approach. However, this method would require a flexible substrate, such as PDMS which can not be annealed above 300 °C [108]. If the setup is compact enough to fit within an inverted microscope or Raman spectrometer, in-situ measurements could be conducted. Similar experiments have been performed with MoS_2 by Castellanos-Gomez et al. [63].

References

[1] J. Van Ginkel, M. Filius, M. Szczepaniak, P. Tulinski, A. S. Meyer, and C. Joo, "Single-molecule peptide fingerprinting," *Proceedings of the National Academy of Sciences*, vol. 115, no. 13, pp. 3338–3343, 2018.

[2] T. Ha, "Single-molecule fluorescence resonance energy transfer," *Methods*, vol. 25, no. 1, pp. 78–86, 2001.

[3] D. H. Shin, X. Yang, and S. Caneva, "Single-molecule protein fingerprinting with photonic hexagonal boron nitride nanopores," *Accounts of Materials Research*, vol. 4, no. 4, pp. 307–310, 2023.

[4] T. T. Tran, K. Bray, M. J. Ford, M. Toth, and I. Aharonovich, "Quantum emission from hexagonal boron nitride monolayers," *Nature nanotechnology*, vol. 11, no. 1, pp. 37–41, 2016.

[5] J. F. W. Herschel, "On a case of superficial colour presented by a homogeneous liquid internally colourless," *Philosophical Transactions of the Royal Society of London*, vol. 135, pp. 143–145, 1845.

[6] "Franck–condon principle," 2019. DOI: doi:10.1351/goldbook.F02510. [Online]. Available: https://doi.org/10.1351/goldbook.F02510.

[7] K. N. Shinde, S. Dhoble, H. Swart, *et al.*, "Basic mechanisms of photoluminescence," *Phosphate Phosphors for Solid-State Lighting*, pp. 41–59, 2012.

[8] G. G. Stokes, "On the change of refrangibility of light," *Philosophical transactions of the Royal Society of London*, no. 142, pp. 463–562, 1852.

[9] H. Rabbani-Haghighi, "New materials and device architectures for organic solid-state lasers," Ph.D. dissertation, Université Paris-Nord-Paris XIII, 2011.

[10] *What is a jablonski diagram (perrin-jablonski diagram)?* https://www.edinst.com/blog/jablonski-diagram-2/, Accessed: 31-12-2023.

[11] M. Kasha, "Characterization of electronic transitions in complex molecules," *Discussions of the Faraday society*, vol. 9, pp. 14–19, 1950.

[12] J. R. Lakowicz, *Principles of fluorescence spectroscopy*. Kluwer Academic/Plenum, 1999.

[13] S. A. Hussain, "An introduction to fluorescence resonance energy transfer (fret)," *arXiv preprint arXiv:0908.1815*, 2009.

[14] P. R. Selvin, "The renaissance of fluorescence resonance energy transfer," *Nature structural biology*, vol. 7, no. 9, pp. 730–734, 2000.

[15] L. Yuan, W. Lin, K. Zheng, and S. Zhu, "Fret-based small-molecule fluorescent probes: Rational design and bioimaging applications," *Accounts of chemical research*, vol. 46, no. 7, pp. 1462–1473, 2013.

[16] A. M. Eagleton, "Genetically engineered peptides for light harvesting and folding kinetics studies," 2018.

[17] M. Kianinia, Z.-Q. Xu, M. Toth, and I. Aharonovich, "Quantum emitters in 2d materials: Emitter engineering, photophysics, and integration in photonic nanostructures," *Applied Physics Reviews*, vol. 9, no. 1, 2022.

[18] I. Aharonovich and M. Toth, "Quantum emitters in two dimensions," *Science*, vol. 358, no. 6360, pp. 170–171, 2017.

[19] I. Aharonovich and E. Neu, "Diamond nanophotonics," *Advanced Optical Materials*, vol. 2, no. 10, pp. 911–928, 2014.

[20] I. Aharonovich, D. Englund, and M. Toth, "Solid-state single-photon emitters," *Nature photonics*, vol. 10, no. 10, pp. 631–641, 2016.

[21] S. Lagomarsino, A. M. Flatae, S. Sciortino, *et al.*, "Optical properties of silicon-vacancy color centers in diamond created by ion implantation and post-annealing," *Diamond and Related Materials*, vol. 84, pp. 196–203, 2018.

[22] M. G. Dastidar, I. Thekkooden, P. K. Nayak, and V. P. Bhallamudi, "Quantum emitters and detectors based on 2d van der waals materials," *Nanoscale*, vol. 14, no. 14, pp. 5289–5313, 2022.

[23] *Phonon-energy-diagram*, `https://upload.wikimedia.org/wikipedia/commons/6/6a/Phonon-energy-diagram.png`, Accessed: 26-01-2024.

[24] Z.-Q. Xu, N. Mendelson, J. A. Scott, C. Li, I. Aharonovich, and M. Toth, "Charge transition levels of quantum emitters in hexagonal boron nitride," *arXiv preprint arXiv:1907.00471*, 2019.

[25] Z. Xiong, L. Zhong, H. Wang, and X. Li, "Structural defects, mechanical behaviors, and properties of two-dimensional materials," *Materials*, vol. 14, no. 5, p. 1192, 2021.

[26] K. Novoselov, A. Mishchenko, A. Carvalho, and A. Castro Neto, "2d materials and van der waals heterostructures," *Science*, vol. 353, no. 6298, aac9439, 2016.

[27] W. Choi, N. Choudhary, G. H. Han, J. Park, D. Akinwande, and Y. H. Lee, "Recent development of two-dimensional transition metal dichalcogenides and their applications," *Materials Today*, vol. 20, no. 3, pp. 116–130, 2017.

[28] *Tungsten diselenide (wse2) powder and crystal*, `https://www.ossila.com/products/tungsten-diselenide`, Accessed: 31-01-2024.

[29] B. Radisavljevic, A. Radenovic, J. Brivio, V. Giacometti, and A. Kis, "Single-layer mos2 transistors," *Nature nanotechnology*, vol. 6, no. 3, pp. 147–150, 2011.

[30] O. Lopez-Sanchez, D. Lembke, M. Kayci, A. Radenovic, and A. Kis, "Ultrasensitive photodetectors based on monolayer mos2," *Nature nanotechnology*, vol. 8, no. 7, pp. 497–501, 2013.

[31] S. Bertolazzi, J. Brivio, and A. Kis, "Stretching and breaking of ultrathin mos2," *ACS nano*, vol. 5, no. 12, pp. 9703–9709, 2011.

[32] A. Bolotsky, D. Butler, C. Dong, *et al.*, "Two-dimensional materials in biosensing and healthcare: From in vitro diagnostics to optogenetics and beyond," *ACS nano*, vol. 13, no. 9, pp. 9781–9810, 2019.

[33] M. J. Molaei, M. Younas, and M. Rezakazemi, "A comprehensive review on recent advances in two-dimensional (2d) hexagonal boron nitride," *ACS Applied Electronic Materials*, vol. 3, no. 12, pp. 5165–5187, 2021.

[34] Y. Lin and J. W. Connell, "Advances in 2d boron nitride nanostructures: Nanosheets, nanoribbons, nanomeshes, and hybrids with graphene," *Nanoscale*, vol. 4, no. 22, pp. 6908–6939, 2012.

[35] *The structure of hexagonal boron nitride*, `https://www.ossila.com/products/hexagonal-boron-nitride`, Accessed: 01-01-2024.

[36] G. Cassabois, P. Valvin, and B. Gil, "Hexagonal boron nitride is an indirect bandgap semiconductor," *Nature photonics*, vol. 10, no. 4, pp. 262–266, 2016.

[37] T. T. Tran, C. Elbadawi, D. Totonjian, *et al.*, "Robust multicolor single photon emission from point defects in hexagonal boron nitride," *ACS nano*, vol. 10, no. 8, pp. 7331–7338, 2016.

[38] A. Falin, Q. Cai, E. J. Santos, *et al.*, "Mechanical properties of atomically thin boron nitride and the role of interlayer interactions," *Nature communications*, vol. 8, no. 1, p. 15 815, 2017.

[39] P. Tonndorf, R. Schmidt, P. Böttger, *et al.*, "Photoluminescence emission and raman response of monolayer mos 2, mose 2, and wse 2," *Optics express*, vol. 21, no. 4, pp. 4908–4916, 2013.

[40] X. Zhang, D. Sun, Y. Li, *et al.*, "Measurement of lateral and interfacial thermal conductivity of single-and bilayer mos2 and mose2 using refined optothermal raman technique," *ACS applied materials & interfaces*, vol. 7, no. 46, pp. 25 923–25 929, 2015.

[41] L. Zhang, Z. Lu, Y. Song, *et al.*, "Thermal expansion coefficient of monolayer molybdenum disulfide using micro-raman spectroscopy," *Nano letters*, vol. 19, no. 7, pp. 4745–4751, 2019.

[42] R. Yan, J. R. Simpson, S. Bertolazzi, *et al.*, "Thermal conductivity of monolayer molybdenum disulfide obtained from temperature-dependent raman spectroscopy," *ACS nano*, vol. 8, no. 1, pp. 986–993, 2014.

[43] Z. Yan, J. Lin, Z. Peng, *et al.*, "Toward the synthesis of wafer-scale single-crystal graphene on copper foils," *ACS nano*, vol. 6, no. 10, pp. 9110–9117, 2012.

[44] K. Novoselov and A. C. Neto, "Two-dimensional crystals-based heterostructures: Materials with tailored properties," *Physica Scripta*, vol. 2012, no. T146, p. 014 006, 2012.

[45] K. S. Novoselov, A. K. Geim, S. V. Morozov, *et al.*, "Electric field effect in atomically thin carbon films," *science*, vol. 306, no. 5696, pp. 666–669, 2004.

[46] G. Wang and N. Fang, "Detecting and tracking nonfluorescent nanoparticle probes in live cells," *Methods in enzymology*, vol. 504, pp. 83–108, 2012.

[47] *Illumination techniques in optical microscopy*, `https://www.edinst.com/blog/illumination-techniques-in-optical-microscopy/`, Accessed: 17-04-2024.

[48] I. Rousso and A. Deshpande, "Applications of atomic force microscopy in hiv-1 research," *Viruses*, vol. 14, no. 3, p. 648, 2022.

[49] *Scanning electron microscopy (sem)*, `https://www.ugent.be/ea/match/sms/en/services/material_analysis.htm`.

[50] *Scanning electron microscope*, `https://www.britannica.com/technology/scanning-electron-microscope`.

[51] M. Kuvshinov, "Development and application of gas-phase raman spectroscopy techniques for analysis of carbon nanotube synthesis processes," Ph.D. dissertation, 2021.

[52] *Raman spectroscopy academy*, `https://www.thermofisher.com/nl/en/home/industrial/spectroscopy-elemental-isotope-analysis/molecular-spectroscopy/raman-microscopy/resources/raman-spectroscopy-academy.html`, Accessed: 17-04-2024.

[53] I. Stenger, L. Schué, M. Boukhicha, *et al.*, "Low frequency raman spectroscopy of few-atomic-layer thick hbn crystals," *2D Materials*, vol. 4, no. 3, p. 031 003, 2017.

[54] M. Krečmarová, D. Andres-Penares, L. Fekete, *et al.*, "Optical contrast and raman spectroscopy techniques applied to few-layer 2d hexagonal boron nitride," *Nanomaterials*, vol. 9, no. 7, p. 1047, 2019.

[55] S. Reich, A. Ferrari, R. Arenal, A. Loiseau, I. Bello, and J. Robertson, "Resonant raman scattering in cubic and hexagonal boron nitride," *Physical Review B—Condensed Matter and Materials Physics*, vol. 71, no. 20, p. 205 201, 2005.

[56] K. Bera, D. Chugh, A. Patra, H. H. Tan, C. Jagadish, and A. Roy, "Strain distribution in wrinkled hbn films," *Solid State Communications*, vol. 310, p. 113 847, 2020.

[57] E. Blundo, A. Surrente, D. Spirito, *et al.*, "Vibrational properties in highly strained hexagonal boron nitride bubbles," *Nano letters*, vol. 22, no. 4, pp. 1525–1533, 2022.

[58] T. Mohiuddin, A. Lombardo, R. Nair, *et al.*, "Uniaxial strain in graphene by raman spectroscopy: G peak splitting, grüneisen parameters, and sample orientation," *Physical Review B—Condensed Matter and Materials Physics*, vol. 79, no. 20, p. 205 433, 2009.

[59] M. Koperski, K. Nogajewski, A. Arora, *et al.*, "Single photon emitters in exfoliated wse2 structures," *Nature nanotechnology*, vol. 10, no. 6, pp. 503–506, 2015.

[60] C. Chakraborty, L. Kinnischtzke, K. M. Goodfellow, R. Beams, and A. N. Vamivakas, "Voltage-controlled quantum light from an atomically thin semiconductor," *Nature nanotechnology*, vol. 10, no. 6, pp. 507–511, 2015.

[61] P. Tonndorf, R. Schmidt, R. Schneider, *et al.*, "Single-photon emission from localized excitons in an atomically thin semiconductor," *Optica*, vol. 2, no. 4, pp. 347–352, 2015.

[62] J. Feng, X. Qian, C.-W. Huang, and J. Li, "Strain-engineered artificial atom as a broad-spectrum solar energy funnel," *Nature Photonics*, vol. 6, no. 12, pp. 866–872, 2012.

[63] A. Castellanos-Gomez, R. Roldán, E. Cappelluti, *et al.*, "Local strain engineering in atomically thin mos2," *Nano letters*, vol. 13, no. 11, pp. 5361–5366, 2013.

[64] S. A. Tawfik, S. Ali, M. Fronzi, *et al.*, "First-principles investigation of quantum emission from hbn defects," *Nanoscale*, vol. 9, no. 36, pp. 13 575–13 582, 2017.

[65] R. Bourrellier, S. Meuret, A. Tararan, *et al.*, "Bright uv single photon emission at point defects in h-bn," *Nano letters*, vol. 16, no. 7, pp. 4317–4321, 2016.

[66] N. Mendelson, D. Chugh, J. R. Reimers, *et al.*, "Identifying carbon as the source of visible single-photon emission from hexagonal boron nitride," *Nature materials*, vol. 20, no. 3, pp. 321–328, 2021.

[67] Z.-Q. Xu, C. Elbadawi, T. T. Tran, *et al.*, "Single photon emission from plasma treated 2d hexagonal boron nitride," *Nanoscale*, vol. 10, no. 17, pp. 7957–7965, 2018.

[68] Y. Luo, N. Liu, X. Li, J. C. Hone, and S. Strauf, "Single photon emission in wse2 up 160 k by quantum yield control," *2D Materials*, vol. 6, no. 3, p. 035 017, 2019.

[69] H. Kim, G. H. Ahn, J. Cho, *et al.*, "Synthetic wse2 monolayers with high photoluminescence quantum yield," *Science advances*, vol. 5, no. 1, eaau4728, 2019.

[70] M. Amani, D.-H. Lien, D. Kiriya, *et al.*, "Near-unity photoluminescence quantum yield in mos2," *Science*, vol. 350, no. 6264, pp. 1065–1068, 2015.

[71] N. Nikolay, N. Mendelson, E. Özelci, *et al.*, "Direct measurement of quantum efficiency of single-photon emitters in hexagonal boron nitride," *Optica*, vol. 6, no. 8, pp. 1084–1088, 2019.

[72] G. Grosso, H. Moon, B. Lienhard, *et al.*, "Tunable and high-purity room temperature single-photon emission from atomic defects in hexagonal boron nitride," *Nature communications*, vol. 8, no. 1, pp. 1–8, 2017.

[73] E. Blundo, E. Cappelluti, M. Felici, G. Pettinari, and A. Polimeni, "Strain-tuning of the electronic, optical, and vibrational properties of two-dimensional crystals," *Applied Physics Reviews*, vol. 8, no. 2, 2021.

[74] N. Mendelson, M. Doherty, M. Toth, I. Aharonovich, and T. T. Tran, "Strain-induced modification of the optical characteristics of quantum emitters in hexagonal boron nitride," *Advanced Materials*, vol. 32, no. 21, p. 1 908 316, 2020.

[75] N. V. Proscia, Z. Shotan, H. Jayakumar, *et al.*, "Near-deterministic activation of room-temperature quantum emitters in hexagonal boron nitride," *Optica*, vol. 5, no. 9, pp. 1128–1134, 2018.

[76] X. Chen, X. Yue, L. Zhang, *et al.*, "Activated single photon emitters and enhanced deep-level emissions in hexagonal boron nitride strain crystal," *Advanced Functional Materials*, vol. 34, no. 1, p. 2 306 128, 2024.

[77] X. Chen, X. Yue, L. Zhang, *et al.*, "Activated single photon emitters and enhanced deep-level emissions in hexagonal boron nitride strain crystal," *Advanced Functional Materials*, p. 2 306 128, 2023.

[78] C. K. Oliveira, E. F. Gomes, M. C. Prado, *et al.*, "Crystal-oriented wrinkles with origami-type junctions in few-layer hexagonal boron nitride," *Nano Research*, vol. 8, pp. 1680–1688, 2015.

[79] L. Chen, K. Elibol, H. Cai, *et al.*, "Direct observation of layer-stacking and oriented wrinkles in multilayer hexagonal boron nitride," *2D Materials*, vol. 8, no. 2, p. 024 001, 2021.

[80] D. Yim, M. Yu, G. Noh, J. Lee, and H. Seo, "Polarization and localization of single-photon emitters in hexagonal boron nitride wrinkles," *ACS applied materials & interfaces*, vol. 12, no. 32, pp. 36 362–36 369, 2020.

[81] S. Yang, C. Wang, H. Sahin, *et al.*, "Tuning the optical, magnetic, and electrical properties of rese2 by nanoscale strain engineering," *Nano letters*, vol. 15, no. 3, pp. 1660–1666, 2015.

[82] Y. Anzai, M. Yamamoto, S. Genchi, *et al.*, "Broad range thickness identification of hexagonal boron nitride by colors," *Applied physics express*, vol. 12, no. 5, p. 055 007, 2019.

[83] W. Paszkowicz, J. Pelka, M. Knapp, T. Szyszko, and S. Podsiadlo, "Lattice parameters and anisotropic thermal expansion of hexagonal boron nitride in the 10–297.5 k temperature range," *Applied Physics A*, vol. 75, pp. 431–435, 2002.

[84] *Understanding the thermal conductivity of silicon*, `https://www.iue.tuwien.ac.at/phd/filipovic/node26.html`.

[85] *Silicon dioxide properties*, `https://www.iue.tuwien.ac.at/phd/filipovic/node26.html`.

[86] *Technical information for type ge 124 fused quartz*, https://www.microtonano.com/TSB-type-GE-124-fused-quartz.php.

[87] *Sapphire substrate 5x5mm, double sided polished, pk 5*, https://www.2spi.com/item/499ss5x5-ab/sapphire-substate/.

[88] N. Chejanovsky, M. Rezai, F. Paolucci, *et al.*, "Structural attributes and photodynamics of visible spectrum quantum emitters in hexagonal boron nitride," *Nano letters*, vol. 16, no. 11, pp. 7037–7045, 2016.

[89] T. Vogl, G. Campbell, B. C. Buchler, Y. Lu, and P. K. Lam, "Fabrication and deterministic transfer of high-quality quantum emitters in hexagonal boron nitride," *Acs Photonics*, vol. 5, no. 6, pp. 2305–2312, 2018.

[90] M. D. Abràmoff, P. J. Magalhães, and S. J. Ram, "Image processing with imagej," *Biophotonics international*, vol. 11, no. 7, pp. 36–42, 2004.

[91] *Streamhr™: Generate high resolution chemical images*, https://www.renishaw.com/en/streamhr-generate-high-resolution-chemical-images--25501?srsltid=AfmBOop9NGSbjzf8zuYQiEWYnymAihsJPjDQoaqfekMBCVXC1zqg2g0l.

[92] P. Ares, Y. B. Wang, C. R. Woods, *et al.*, "Van der waals interaction affects wrinkle formation in two-dimensional materials," *Proceedings of the National Academy of Sciences*, vol. 118, no. 14, e2025870118, 2021.

[93] G. Zhang, Y. Chang, and B. Yan, "The study of the wrinkles of hexagonal boron-nitride flake after the annealing," *Crystals*, vol. 13, no. 2, p. 304, 2023.

[94] N. Marom, J. Bernstein, J. Garel, *et al.*, "Stacking and registry effects in layered materials: The case of hexagonal boron nitride," *Physical review letters*, vol. 105, no. 4, p. 046 801, 2010.

[95] W. Wang, Z. Li, A. J. Marsden, M. A. Bissett, and R. J. Young, "Interlayer and interfacial stress transfer in hbn nanosheets," *2D Materials*, vol. 8, no. 3, p. 035 058, 2021.

[96] B. Xu, N. Mao, Y. Zhao, L. Tong, and J. Zhang, "Polarized raman spectroscopy for determining crystallographic orientation of low-dimensional materials," *The Journal of Physical Chemistry Letters*, vol. 12, no. 31, pp. 7442–7452, 2021.

[97] C. Cong, T. Yu, and H. Wang, "Raman study on the g mode of graphene for determination of edge orientation," *ACS nano*, vol. 4, no. 6, pp. 3175–3180, 2010.

[98] C. Casiraghi, A. Hartschuh, H. Qian, *et al.*, "Raman spectroscopy of graphene edges," *Nano letters*, vol. 9, no. 4, pp. 1433–1441, 2009.

[99] C. Androulidakis, E. Koukaras, M. Poss, K. Papagelis, C. Galiotis, and S. Tawfick, "Strained hexagonal boron nitride: Phonon shift and grüneisen parameter," *Physical Review B*, vol. 97, no. 24, p. 241 414, 2018.

[100] L. Schué, I. Stenger, F. Fossard, A. Loiseau, and J. Barjon, "Characterization methods dedicated to nanometer-thick hbn layers," *2D Materials*, vol. 4, no. 1, p. 015 028, 2016.

[101] Q. Cai, D. Scullion, A. Falin, *et al.*, "Raman signature and phonon dispersion of atomically thin boron nitride," *Nanoscale*, vol. 9, no. 9, pp. 3059–3067, 2017.

[102] R. Cuscó, J. H. Edgar, S. Liu, J. Li, and L. Artús, "Isotopic disorder: The prevailing mechanism in limiting the phonon lifetime in hexagonal bn," *Physical Review Letters*, vol. 124, no. 16, p. 167 402, 2020.

[103] K. Bera, D. Chugh, A. Patra, H. H. Tan, and C. Roy, "Strain distribution and thermal strain relaxation in movpe grown hbn films on sapphire substrates," *arXiv preprint arXiv:1907.05591*, 2019.

[104] N. Ronceray, Y. You, E. Glushkov, *et al.*, "Liquid-activated quantum emission from pristine hexagonal boron nitride for nanofluidic sensing," *Nature Materials*, vol. 22, no. 10, pp. 1236–1242, 2023.

[105] R. V. Kamat, A. L. Sharpe, M. Pendharkar, *et al.*, "Deterministic fabrication of graphene hexagonal boron nitride moiré superlattices," *Proceedings of the National Academy of Sciences*, vol. 121, no. 40, e2410993121, 2024.

[106] K. Morikawa, Y. Kazoe, K. Mawatari, T. Tsukahara, and T. Kitamori, "Dielectric constant of liquids confined in the extended nanospace measured by a streaming potential method," *Analytical chemistry*, vol. 87, no. 3, pp. 1475–1479, 2015.

[107] L. Meng, Y. Li, T. S. Liu, *et al.*, "Wrinkle networks in exfoliated multilayer graphene and other layered materials," *Carbon*, vol. 156, pp. 24–30, 2020.

[108] N. Grassie and I. Macfarlane, "The thermal degradation of polysiloxanes—i. poly (dimethylsiloxane)," *European polymer journal*, vol. 14, no. 11, pp. 875–884, 1978.

A

Appendix A

A.1. Pre-annealing to remove contamination

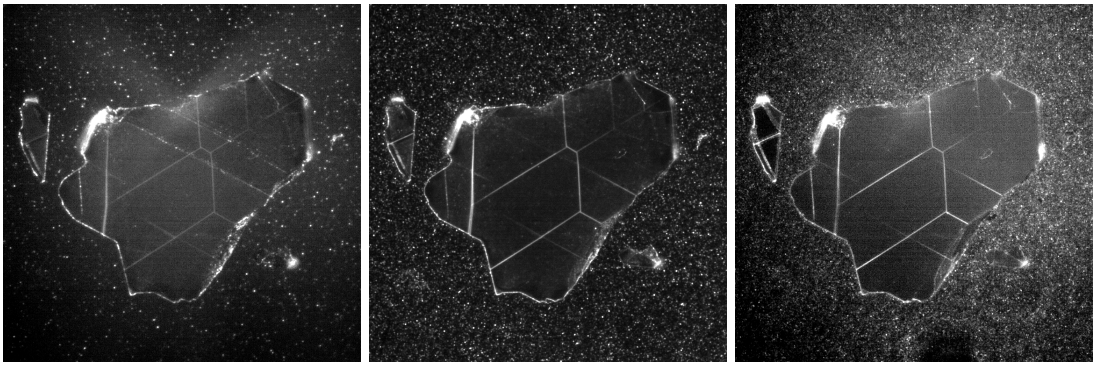

(a) (b) (c)

Figure A.1: Fluorescence microscopy images of contaminated samples in three different excitation wavelengths: **(a)** Red laser (635 nm) **(b)** Green **(c)** Blue laser (488 nm).

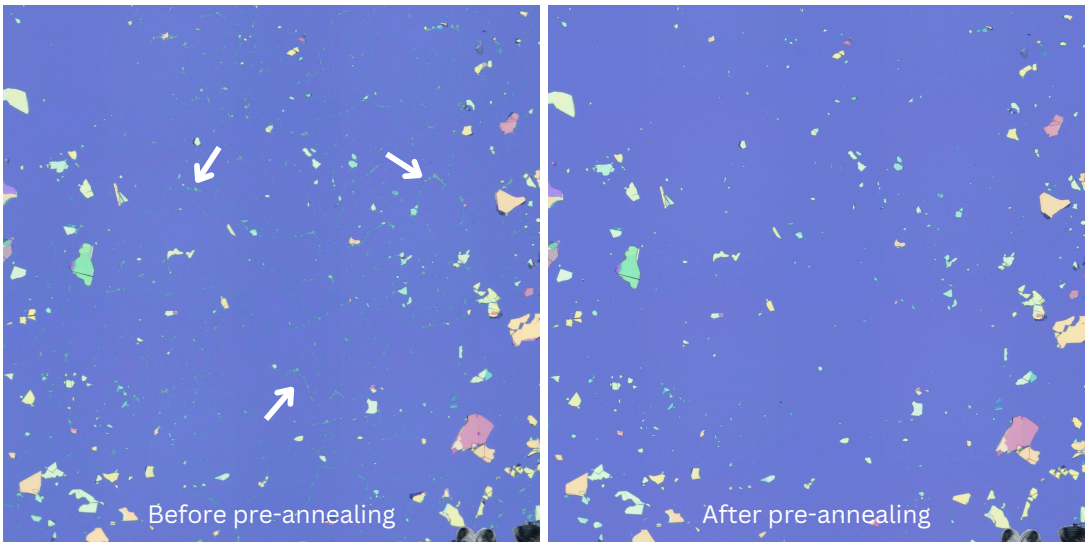

(a) (b)

Figure A.2: Si/SiO_2 substrate with exfoliated h-BN flakes before **(a)** after **(b)** pre-annealing on a hotplate for 10 minutes at 450 °C. The white arrows in **(a)** point out glue residues from tape exfoliation.